

T-2873

Sample Preparation and Characterization
Study of CdSnP_2

by

John R. Tuttle

ProQuest Number: 10782566

All rights reserved

INFORMATION TO ALL USERS

The quality of this reproduction is dependent upon the quality of the copy submitted.

In the unlikely event that the author did not send a complete manuscript and there are missing pages, these will be noted. Also, if material had to be removed, a note will indicate the deletion.



ProQuest 10782566

Published by ProQuest LLC (2018). Copyright of the Dissertation is held by the Author.

All rights reserved.

This work is protected against unauthorized copying under Title 17, United States Code
Microform Edition © ProQuest LLC.

ProQuest LLC.
789 East Eisenhower Parkway
P.O. Box 1346
Ann Arbor, MI 48106 – 1346

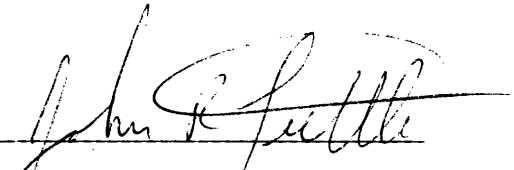
T-2873

A thesis submitted to the Faculty and the Board of Trustees of the Colorado School of Mines in partial fulfillment of the requirements for the degree of Master of Science, Physics.

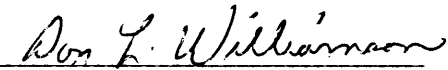
Golden, Colorado

Date Jan 23, 1984

Signed:


John R. Tuttle

Approved:

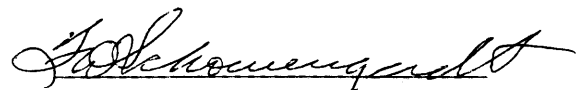


Dr. D. L. Williamson

Thesis Advisor

Golden, Colorado

Date 1/23/84



Dr. F. D. Schewengerdt

Head of Department of

Physics

ABSTRACT

A sample preparation and characterization study was conducted on the II-IV-V₂ ternary chalcopyrite semiconducting material CdSnP₂ to determine its potential for use in photoelectrochemical (PEC) cells. Single crystals were grown in 90 mol % Sn solution by the precipitation method and their properties investigated. Several samples were doped with .1 to .5 mol % Cu to produce p-CdSnP₂, and their properties investigated.

Single crystal size can be increased through temperature profiling (spiking) and nucleation controlled by introducing "heat-sinks" on the ampoule surface. Crystal morphologies and sizes ranged from needle-like with .1 × .1 mm² cross-sections, to multiply layered plate-like with 5 × 2 mm² cross-sections. Layered and stacked crystals were highly resistive front to back due to twin boundaries and open inclusions.

Structural characterization by x-ray diffraction (XRD) substantiated the tetrahedrally coordinated chalcopyrite structure ($I\bar{4}2d$ space group) with lattice constants $a = 5.900 \text{ \AA}$ and $c = 11.513 \text{ \AA}$. XRD also identified Sn₄P₃ precipitates in each crystal yield. Structure factor calculations verified the allowed (hkl) values for diffraction peak maxima, and further indicated a similarity

in the valence electron levels of Sn and Cd due to the apparent equality of their atomic form factors.

Mössbauer effect spectroscopy (MES) studies indicated a tetrahedral coordination in the Sn sublattice and the existence of sp^3 hybrid orbitals in the valence band. Further MES studies showed the presence of ≈ 1 mole % of Sn_4P_3 inclusions in only $CdSnP_2:Cu$ crystals. No reasonable explanation for the phenomena can be provided at this time.

Photoelectrochemical characterization incorporated $CdSnP_2$ single crystals as semiconductor electrodes in PEC cells. Several redox solutions were tested with polysulfide giving the best results. Various characteristic material properties, plus values for the flat-band potential and cell efficiency are reported for n- $CdSnP_2$. Results for $CdSnP_2:Cu$ in the same configuration were both inconclusive and contradictory. Several samples exhibited both types of conductivity. It should be noted that these measurements on $CdSnP_2$ are the first of their kind.

The future of n- $CdSnP_2$ as a semiconductor electrode in PEC cell configuration is promising. $CdSnP_2:Cu$, on the other hand, does not show much promise as a semiconductor electrode.

T-2873

Further studies to increase single crystal size, to realize p-type conductivity, and to determine optimal redox solutions should be conducted.

TABLE OF CONTENTS

| | <u>Page</u> |
|--|-------------|
| Abstract..... | iii |
| List of Tables..... | viii |
| List of Illustrations..... | ix |
| Acknowledgements..... | xi |
| Introduction..... | 1 |
| 1. Ternary Chalcopyrites..... | 5 |
| 2. Sample Preparation..... | 8 |
| 2.1 Theory..... | 10 |
| 2.2 Experimental Procedure..... | 16 |
| 2.2.1 Experimental Set Up..... | 17 |
| 2.2.2 Crystal Growth and Extraction..... | 19 |
| 2.3 Results and Discussion..... | 24 |
| 3. Structural Characterization..... | 29 |
| 3.1 General Properties of Chalcopyrites..... | 30 |
| 3.2 X-ray Diffraction..... | 33 |
| 3.2.1 Theory..... | 34 |
| 3.2.2 Experimental Procedure..... | 42 |
| 3.2.3 Results and Discussion..... | 43 |
| 3.3 Mössbauer Effect Spectroscopy..... | 46 |
| 3.3.1 Theory..... | 47 |
| 3.3.2 Experimental Procedure..... | 52 |
| 3.3.3 Results and Discussion..... | 55 |

| | |
|---|----|
| 4. Photoelectrochemical Characterization..... | 59 |
| 4.1 PEC Theory..... | 61 |
| 4.2 Experimental Procedure..... | 71 |
| 4.3 Results and Discussion..... | 75 |
| 5. Conclusion..... | 90 |
| References..... | 93 |
| Appendix 1 - Structure Factor Derivation..... | 97 |

LIST OF TABLES

| | <u>Page</u> |
|--|-------------|
| 2.1 CdSnP ₂ Growth Parameters and Crystal Yield Results..... | 20 |
| 3.1 Structure Factor Results for CdSnP ₂ | 39 |
| 3.2 D-spacings and Lattice Parameter Calculations from XRD Data..... | 45 |
| 3.3 Summary of Mössbauer Analysis..... | 56 |
| 4.1 Properties of n-CdSnP ₂ from PEC Characterization..... | 75 |

LIST OF ILLUSTRATIONS

| | <u>Page</u> |
|---|-------------|
| 1.1 Schematic Illustration of the Formation of II-IV-V ₂ Compounds..... | 6 |
| 1.2 Comparison of the Brillouin Zones of the Zinc- Blende and Chalcopyrite Structures..... | 6 |
| 2.1 The CdP ₂ -Sn System..... | 11 |
| 2.2 A Closeup View of Solidus-Liquidus Line in the CdP ₂ -Sn System..... | 12 |
| 2.3 Experimental Set-up and "Heat-Sink" Apparatus | 18 |
| 2.4 Sample Heating Profile and Schedule..... | 21 |
| 2.5 Cooling Profiles..... | 23 |
| 2.6 Photographs of Representative Crystals..... | 28 |
| 3.1 The Tetragonal Chalcopyrite Structure..... | 31 |
| 3.2 CdSnP ₂ d-spacings (JCPDS)..... | 40 |
| 3.3 XRD Data..... | 44 |
| 3.4 Plot of Isomer Shift as a Function of 5s-5p Electrons..... | 51 |
| 3.5 (a)-(f) Mössbauer Spectra..... | 53,54 |
| 4.1 Schematic of Cell Featuring Impedance (Capacitative) Measurement..... | 63 |
| 4.2 Structure of Semiconductor-Electrolyte Interface..... | 63 |

| (Cont'd) | <u>Page</u> |
|--|-------------|
| 4.3 Block Diagram of Experimental Apparatus and Related Electronics..... | 73 |
| 4.4 Mott-Schottky Analysis of n-CdSnP ₂ ($\frac{1}{C^2}$ vs V_{cell})..... | 77 |
| 4.5 Photocurrent Analysis of n-CdSnP ₂ ($J^2(h\nu)^2$ vs $h\nu$) and Description of Transitions..... | 78 |
| 4.6 Photocurrent-Spectroscopy of n-CdSnP ₂ (J vs $h\nu$)..... | 79 |
| 4.7 Photocurrent-Voltage Analysis of n-CdSnP ₂ (J vs V)..... | 79 |
| 4.8 Photocurrent-Voltage Analysis of n-CdSnP ₂ ($\ln(1-\phi)$ vs $\sqrt{V-V_{fb}}$)..... | 81 |
| 4.9 Mott-Schottky Analysis of p-CdSnP ₂ :Cu..... | 83 |
| 4.10 Photocurrent-Spectroscopy of p-CdSnP ₂ :Cu (J vs $h\nu$)..... | 84 |
| 4.11 Sample Resistivity of p-CdSnP ₂ :Cu..... | 86 |
| 4.12 Photocurrent-Voltage Measurements of p-CdSnP ₂ :Cu (J vs V)..... | 86 |
| 4.13 Photocurrent-Voltage Analysis of p-CdSnP ₂ :Cu (J^2 vs V)..... | 88 |
| 4.14 Photocurrent-Voltage Analysis of p-CdSnP ₂ :Cu ($\ln(1-\phi)$ vs $\sqrt{V-V_{fb}}$)..... | 88 |

ACKNOWLEDGEMENTS

I would like to take this opportunity to express my sincere gratitude to my Thesis advisor, Dr. Don L. Williamson, for his support, guidance, and effort in assuring the success of this study and subsequent thesis.

I thank the members of my thesis committee, Dr. Bill Law, for his encouragement and understanding during the rough times, and Dr. John Trefny for his superior academic and intellectual stimulation.

A special thanks goes to Dr. Bruce Parkinson and Dr. Jaap Folmer of the Solar Energy Research Institute for their advice on all aspects of this study and for their continuous efforts in moving this research along.

My gratitude goes to the Graduate School of the Colorado School of Mines for supporting my studies with a Graduate Assistantship.

I am deeply thankful, as well, to my parents, Margaret W. and Raymond E. Tuttle, for providing charitable encouragement and direction throughout my academic career.

I must also thank Don Burke and Martha Zelinka for the early academic training and stimulation they provided.

And, finally, a very special thanks to my good friend, Kären L. Wilson, for just being there when I needed support.

INTRODUCTION

It seems quite unimaginable that it has taken mankind so many years to come to the realization that the sun is a viable source of energy. We were so quick to utilize the land and sea, but the sun seemed mysteriously out of reach. It has only been in the past decade or so that serious consideration has been given to solar energy. As solid state physicists and chemists, we are particularly interested in the conversion of sunlight to direct or stored electrical and chemical energy.

Edmund Becquerel first noted in 1839 (1) that a voltage developed when light was directed onto one of the electrodes in an electrolyte solution. A similar effect was first noticed in a solid, selenium, in 1877 by W. G. Adams and R. E. Day (2). In 1954, researchers turned to the problem of utilizing this photovoltaic effect as a source of power. Almost immediately, six percent efficiencies were realized with silicon. Since then, research efforts to develop materials with theoretical efficiencies well above this mark have been extensive.

Research soon led to a category of semiconductors known as III-V compounds, and then to their ternary analogs, II-IV-V₂ compounds. This thesis deals with the characterization of one such compound; cadmium-tin-

phosphide (CdSnP_2), the ternary analog of indium phosphide (InP). It is necessary to mention these analogies for it was the interest in InP that led to the work on CdSnP_2 . InP shows promise in photoconversion applications. However, the high cost of indium prohibits cost efficiency. It is believed that CdSnP_2 , as well as other ternary compounds, will exhibit equal promise due to their similar semiconductor properties and structure.

There are two specific applications of CdSnP_2 that are of interest here. Firstly, the Photoconversion Branch at the Solar Energy Research Institute (SERI) is investigating the potential application of this compound in a system that uses sunlight to photo-electrolyze water into hydrogen and oxygen; a photoassisted electrolysis (PAE) cell. The hydrogen is to be stored and eventually used as fuel. One thus will have a process which results in the conversion of sunlight to stored chemical energy. Secondly, SERI is investigating the potential for use of CdSnP_2 in photovoltaic and photoelectrochemical (PEC) cells, a process which results in the conversion of sunlight to direct or stored electrical energy.

The research conducted for this thesis was in collaboration with SERI and addressed primarily the PEC cell area of interest. The studies are divided into three

categories: 1) sample preparation, 2) structural characterization, and 3) photoelectrochemical characterization. Sample preparation studies concentrate on methods for enhancing single crystal size and growing p-CdSnP₂. Though our studies were limited to crystal formation through precipitation in tin melts, crystal size enhancement can be achieved by proper temperature profiling. P-type crystals were grown via copper doping and compared with undoped n-type crystals. It is believed that p-type crystals are better suited for electrolysis experiments.

Structural characterization consists of x-ray diffraction (XRD) and Mössbauer effect spectroscopy (MES) studies. XRD gives information regarding crystal structure through d-spacing measurements, and, by comparison with known data, verifies that the crystal is CdSnP₂. Additionally, with XRD, we can identify other phases, if present. Theoretical calculations of d-spacings are also made (Appendix 1) and compared to experiment. ¹¹⁹Sn Mössbauer effect spectroscopy, on the other hand, lends insight into the electronic structure of tin and the local symmetry of the tin sites in the crystal structure. Like XRD it is also able to detect other phases, if present, provided they contain Sn.

Photoelectrochemical characterization of CdSnP_2 includes investigations of photocurrent spectra, photocurrent-voltage, and Mott-Schottky measurements. Such electronic properties as the type (direct vs indirect) and value of the energy gap, the type (p vs n) and concentration of majority carriers, the photoconductivity, and the diffusion length of minority carriers are determined from the photocurrent spectra data. Likewise, the efficiency of the cell, the flat-band potential, and a comparison of redox electrolytes is made from photocurrent-voltage measurements. Finally, Mott-Schottky capacity measurements of the space-charge layer in the semiconductor give independent readings on the values of the flat-band potential, doping density, and carrier type.

With the information thus obtained, conclusions as to the possible photochemical and photoelectrical applications of CdSnP_2 are made.

1. TERNARY CHALCOPYRITES

CdSnP_2 is just one of a large class of ternary compounds exhibiting the (so-called) chalcopyrite crystal structure. These compounds are currently receiving considerable attention because they show promise for applications in such areas as visible and infrared light emitting diodes, non-linear optics, and solar cells (3).

The chalcopyrites have physical properties similar to the well-known diamond, zinc-blende, and wurzite semiconductors due to their tetrahedral coordination. In particular, they are the nearest electronic analogs of the III-V compounds by virtue of each having an electron-atom ratio equal to 4 (Figure 1.1). However, according to Shay and Wernick, the chalcopyrites possess a lower symmetry and exhibit different, though fundamentally similar, band structures than their binary analogs due to three non-cubic aspects of the chalcopyrite structure: 1) a compression of the crystal lattice along the z-axis ($c < 2a$), 2) a distortion of the anion (P) sites away from the $(1/4, 1/4, 1/8)$ and symmetrically related positions, and 3) a doubling of the unit cell in the z-direction resulting from an ordering of two cations (Cd and Sn).

A fair approximation, though, of the band structure for CdSnP_2 is made by imbedding the energy bands of zinc-

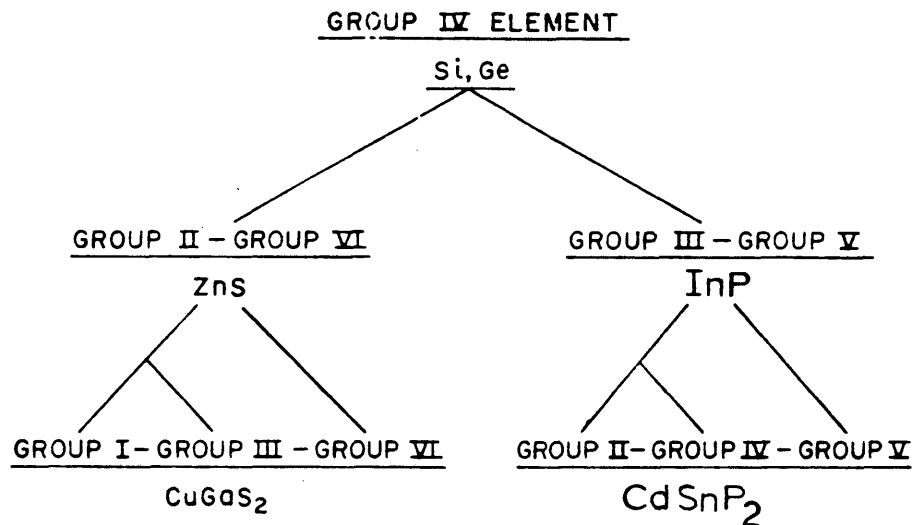


Figure 1.1 Schematic illustration of the formation of I-III-VI₂ and II-IV-V₂ compounds from tetrahedrally coordinated Group IV elements by substitution of elements so as to maintain the electron-atom ratio equal to 4.

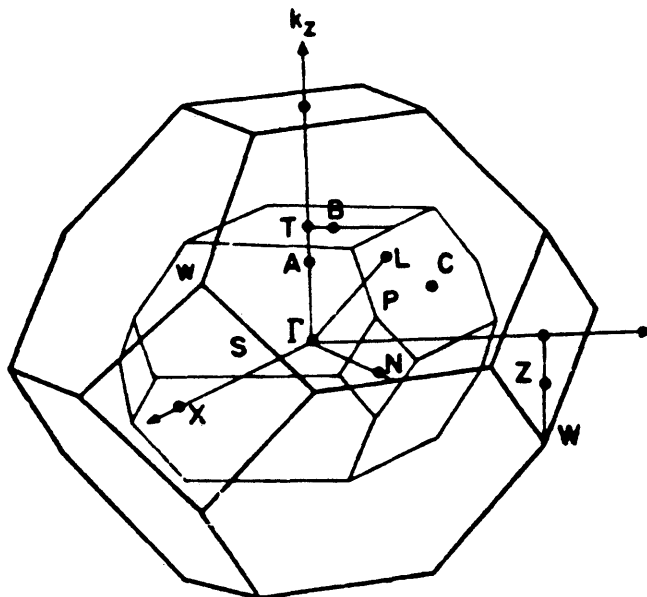


Figure 1.2
Comparison of the Brillouin zones of the zincblende and chalcopyrite lattices.

blende InP into the chalcopyrite brillouin zone (Figure 1.2). This approach has predicted direct energy gaps for CdSnP_2 , which are within ± 0.3 eV of its respective binary analog, InP (4).

For a complete treatise on the twenty known I-III-VI₂ and seventeen known II-IV-V₂ chalcopyrites, refer to (5).

2. SAMPLE PREPARATION

The choice of crystal growth technique for a particular material will depend on many factors (5): the chemical reactivity of the compound and constituent elements, the vapor pressure of constituent elements, the melting point of the compound, and the presence or absence of phase transitions, to name a few. Obviously, knowledge of the phase equilibria for the system determines the final choice of crystal growth technique.

The synthesis and subsequent growth of ternary chalcopyrites can be divided into four principal techniques: (1) direct synthesis from stoichiometric amounts of constituent elements; (2) direct synthesis involving binary compounds of constituent elements; (3) chemical vapor deposition of constituent elements; (4) solution growth by precipitation of the desired compound from a saturated solvent. Since CdSnP_2 melts peritectically [$\text{CdSnP}_2(\text{sol}) \rightleftharpoons \text{CdP}_2(\text{sol}) + \text{liq.}$], it must be grown in a solution of molten tin rather than from a melt of its own composition, which would be faster and preferable (6).

Chemical Vapor Deposition (CVD) and Liquid Phase Epitaxy (LPE) methods have been successful in growing CdSnP_2 on substrates of InP (7). These heterojunctions

have infrared-detection applications as well as possible photovoltaic applications. For more information concerning these and other crystal growth methods for CdSnP_2 and other chalcopyrites, refer to (6), (7).

2.1 Sample Preparation Theory

CdSnP_2 forms peritectically and solution growth is used. Crystals can be grown from dilute solutions in the 90-99 mole % Sn composition range, with the remaining charge consisting of stoichiometric amounts of Cd and P. With this composition, one can, according to the CdP_2 -Sn phase diagram (Figure 2.1), approach the CdSnP_2 phase directly and minimize additional undesired precipitates. Such precipitates include tin-phosphide, Sn_4P_3 , and two forms of cadmium-phosphide, CdP_2 and CdP_4 . These compounds are discussed briefly later.

Precipitation of CdSnP_2 occurs in the following manner (refer to Figure 2.2). At 90 mol % Sn composition and above 570°C , for example, CdP_2 exists in solution of liquid Sn. As the temperature is lowered, $\text{CdP}_2(\text{liq.})$ reacts with Sn (liq.) to form $\text{CdSnP}_2(\text{sol})$. The equilibrium phase relationship variable, $X(T)$, is determined by the intersection of the tie-line with the solidus-liquidus line. At a particular temperature, T , the percentage of CdSnP_2 that has precipitated, given that Y is the initial Sn mol %, is given by the ratio

$$\frac{X(T) - Y}{100 - Y}$$

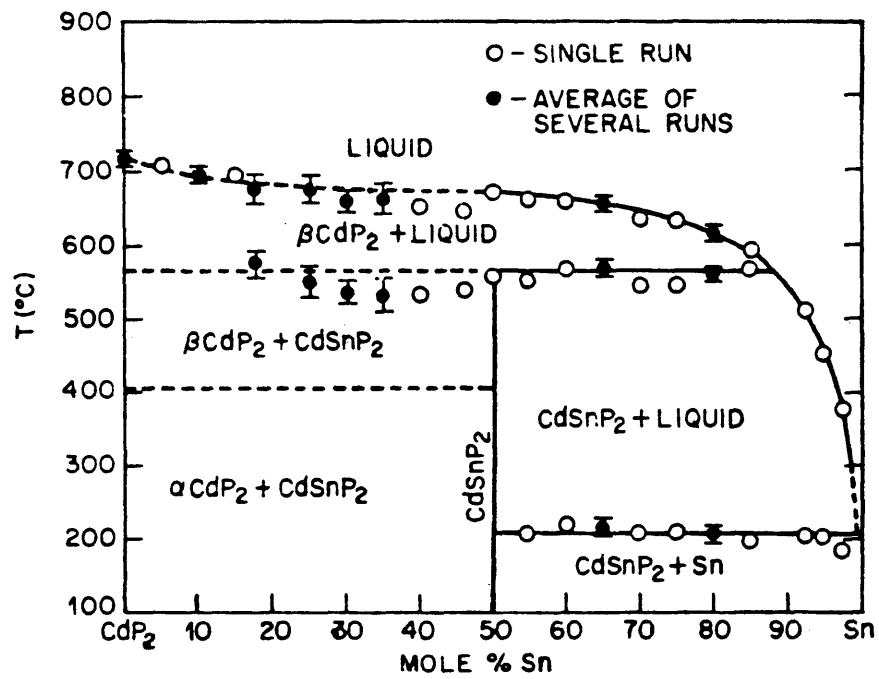


Fig 2.1 The CdP₂-Sn system. (After Buehler *et al.*, 1971.)

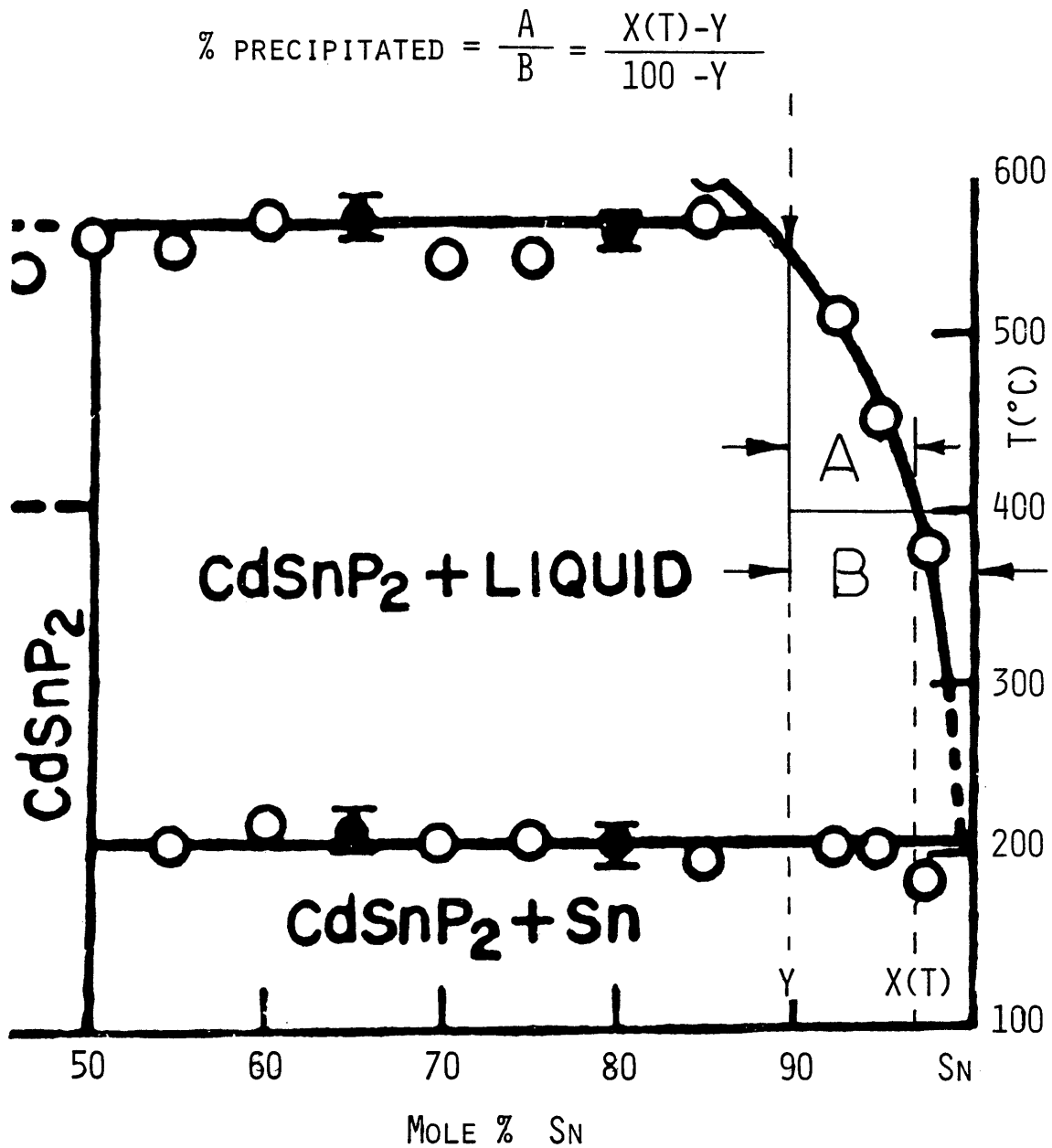


Figure 2.2 A closeup view of the solidus-liquidus line in the CdP₂-Sn system showing method to determine quantity CdSnP₂ precipitated as a function of temperature.

For $Y = 90\%$, and $T = 400^\circ\text{C}$, approximately 67% of the CdSnP_2 has crystallized. It is also apparent that as T decreases, the slope of the L-S line becomes more negative. Consequently, the quantity of CdSnP_2 precipitated per degree change decreases with T .

It is generally recommended (8) that rampdown rates not exceed 80°C per day. However, below 400°C , the rate is not critical for most of the CdSnP_2 has already formed.

Since growth from dilute solutions is primarily dictated by the interplay of nucleation and diffusion, the precipitation in melt technique usually yields small crystals in the range $1\text{-}2 \times .5 \times .5$ mm because nucleation takes place in a random fashion. Thus a part of our crystal growth study included methods to control the number of nucleation sites. Two such methods are temperature profiling and introducing heat sinks on the ampoule surface.

The principle reason for temperature profiling is straightforward. Once the liquid \ddagger CdSnP_2 + liquid phase boundary is reached, precipitation of CdSnP_2 begins. There is, at the start, a variation in the size of the precipitation sites. The goal is to eliminate the smallest precipitates in favor of growing larger crystals by introducing several heating zones or temperature

"spikes." The magnitude and duration of these zones or "spikes" are fairly critical. One would like to raise the temperature fast and far enough so as to dissolve the smallest precipitates, leaving the larger sites to seed further crystal growth. This rate could be determined theoretically if the dissolution kinetics were known. However, this requires knowledge of the extent of solid solubility of CdSnP_2 in Sn, the dependence of the rate of dissolution on surface to volume ratio, and other factors which are beyond the scope of this work. It sufficed to conduct this study on a trial and error basis.

However, one factor which can be discussed relates to the difference between the crystallization temperature as approached from above and the dissolution temperature as approached from below. If the magnitude of the temp rise is not greater than this difference, it will have no effect on the system - i.e., no crystals will dissolve. Since the liquidus and solidus lines in the CdP_2 -Sn system were determined by DTA on a cooling process only, and there is no published material on the reverse process, this difference is not known. But an educated guess, based on the same effect in other materials, puts this difference at between 10 and 40°C. We will, however, only investigate the 10°C to 20°C range to assure that overspiking does not

occur. Several different temperature profiling techniques, at various rates, have been investigated and evaluated to determine which yielded the largest single crystals.

The basis for introducing heat sinks on the ampoule surface is equally straightforward. The introduction of heat sinks produce preferential nucleation sites caused by the decreased solubility of CdSnP_2 in solution in these areas. The heat sinks are merely contacts that are made to conduct heat away from the ampoule surface.

Finally, we are interested in growing both n- and p-type crystals. The undoped CdSnP_2 crystals display n-type conductivity due to a Cd/Sn ratio which shows a slight Sn excess resulting in a high defect concentration of the donor type (9). The existence of multicharge centers (due to lattice defects) that produce acceptor levels is not sufficient compensation. The addition of a copper dopant results in the appearance of new multi-charge centers and increases the degree of compensation to the point where acceptor levels dominate. Quantities of copper ranging from .1 to .5 mol % were added to the charge.

2.2 Experimental Procedure

To test the above theoretical effects of temperature profiling and copper doping on the growth of single crystal CdSnP_2 , and to produce a yield of high quality n- and p-type CdSnP_2 crystals for the purpose of characterization, several samples were prepared. The growth parameters for each run were modified according to the yield of the previous run.

2.2.1 Experimental Set Up

High quality quartz ampoules, designed to include a constriction to ease sealing, were cleaned with chromic acid and H₂O, dried at 200°C, and loaded with 99.999% pure cadmium, red phosphorus, tin, and copper in an inert atmosphere of argon at 1 atm. The ampoules were then evacuated to 2×10^{-6} torr with a liquid nitrogen trapped diffusion pump, and sealed at the constriction with an H₂-O₂ torch. The sealed ampoule was placed in a single zone Lindberg box furnace as shown in Figure 2.3. Temperature control was provided by Lindberg (Eurotherm) digital set point (200-1200°C range) temperature controllers. The controllers were retrofitted with remote/local switches to provide for the option of external computer control. All but the first run incorporated a Leeds and Northrup, 16-region programmable, process programmer with a 10V analog output. All temperatures programmed were scaled to assure compatibility with the 5V analog input for the temperature controller.

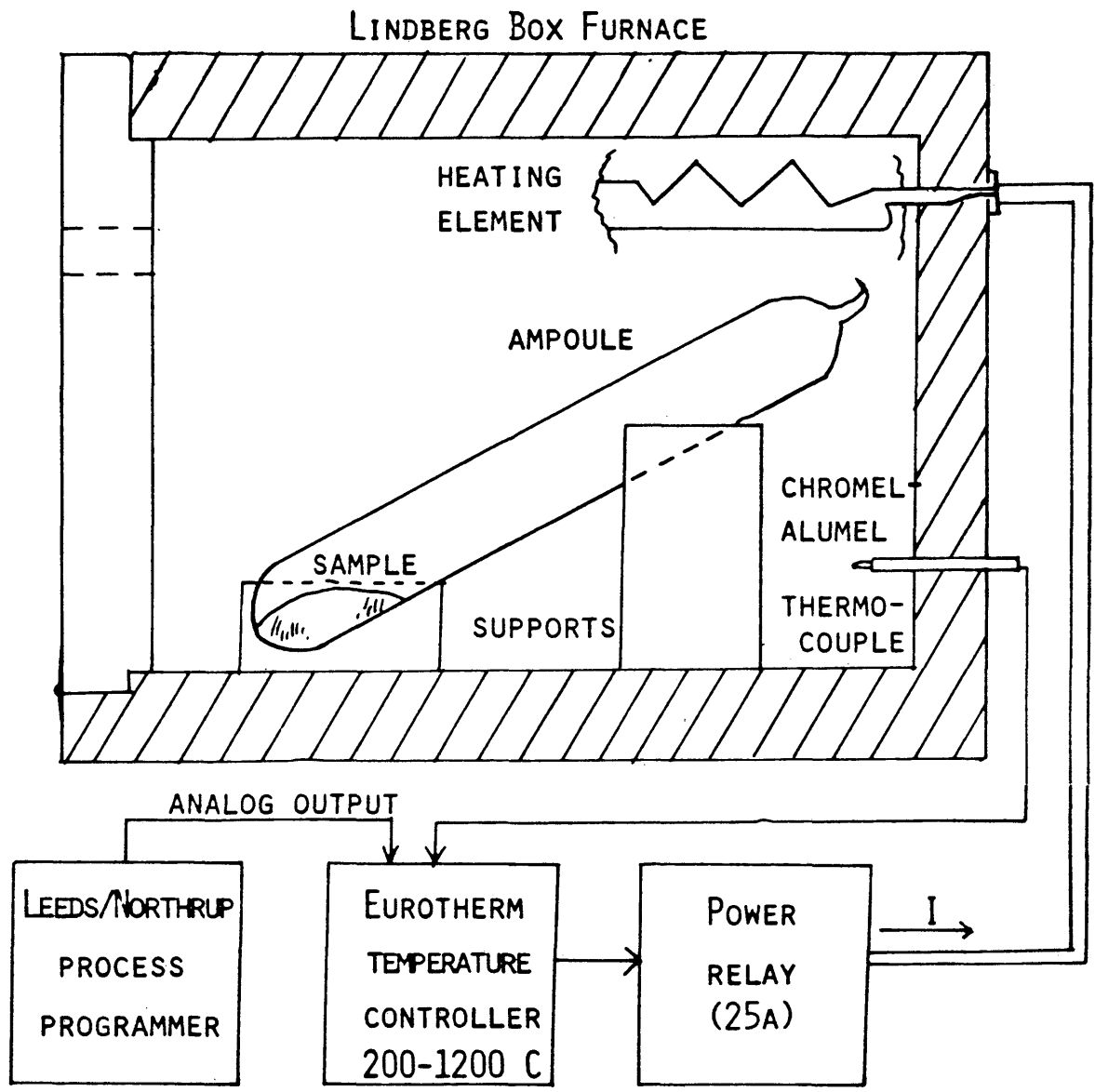
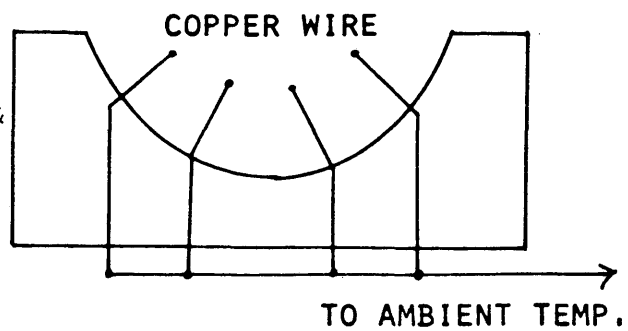


Figure 2.3
Experimental set-up &
heat sink apparatus



2.2.2 Crystal Growth and Extraction

The compositions used for the 6 crystal growth runs are shown in Table 2.1.

Run #1 was accomplished with manual temperature profiling. Consequently, rampdown rates were inconsistent. In any case, the positioning of the ampoule across a furnace zone boundary produced a significant temperature gradient that caused vapor transport of the Cd and P to the cooler end. Consequently, no CdSnP_2 formed.

All subsequent runs were regulated with the process programmer. The heating and soak profile was identical for each run and is shown in Figure 2.4. The sample was heated at a rate of 15°C/hr to 700°C . Slow heating of phosphides is necessary to minimize pressure buildup and excessive heating that results from strongly exothermic reactions. The sample is then held at 700°C for 24 hrs to homogenize the charge. At this temperature, all of the Cd and P react to form CdP_2 . The charge is then cooled very slowly, about 3°C/hr , to the 570°C mark. As briefly discussed earlier, from 570°C to the neighborhood of 400°C is the critical temperature range where approximately 70% of the crystallization process takes place. It is in this range that the nucleation enhancement temperature profiling is

Table 2.1 CdSnP₂ Growth Parameters and Crystal Yield Results

| Run # | Cu (%) | Heat sink Description | Temp Profile (Type, Mag, & Per) | Effective Ramp (°C/hr) | Etch | Crystal Yield Description | Conductivity Type |
|-------|--------|-----------------------|---------------------------------|------------------------|---------------------------------------|--|--------------------|
| 1 | .1% | Ampoule | Manual | -- | -- | Cd and P vapor transported to top of ampoule and formed CdP ₄ needle-like crystals. | -- |
| 2 & 3 | .1% | Furnace floor | Sawtooth 5°, 4 hrs | 2.75°C/hr | HNO ₃ + 5H ₂ O | Large single crystals, on the order of 10 x 4 x 2 mm, with Sn inclusions. Polycrystalline mass at point of contact with furnace. Etchant deposited tin precip. on crystal faces. | Compensated n-type |
| 4 | .1% | Suspended | Sawtooth 5°, 4 hrs | 2.66°C/hr | HNO ₃ + 5H ₂ O | Small single crystals and polycrystals on the order of 4 x 2 x 1 mm, with Sn inclusions. No specific nucleation sites. Etchant left precipitation on surface. | Compensated n-type |
| 5 | 0 | Wire support | Spike 10° & 15° 30 mins. | 5°C/hr | HNO ₃ + H ₂ O | ● Polycrystalline masses at points of contact. Crystals were small and dendritic ~2 x .5 x .2 mm. | n |
| | .5% | Solid block | " | " | " | ● Solid polycrystalline mass with small dendritic growths ~1 x .2 x .1 mm. Etchant strong enough to dissolve tin inclusions but left heavier deposits. | p |
| 6 | 0 | Furnace base | 2-spikes 20°-30 min. | 2.5°C/hr | 4H ₂ O + 3HNO ₃ | ● Majority of crystals grew out from point of contact. Largest crystals were layered or stacked. Sizes - 10 mm x 5 mm x 3 mm. All seem to have open inclusions. HF added to dissolve surface contaminants. | n & p |
| | .5% | " | " | " | + HF | | |

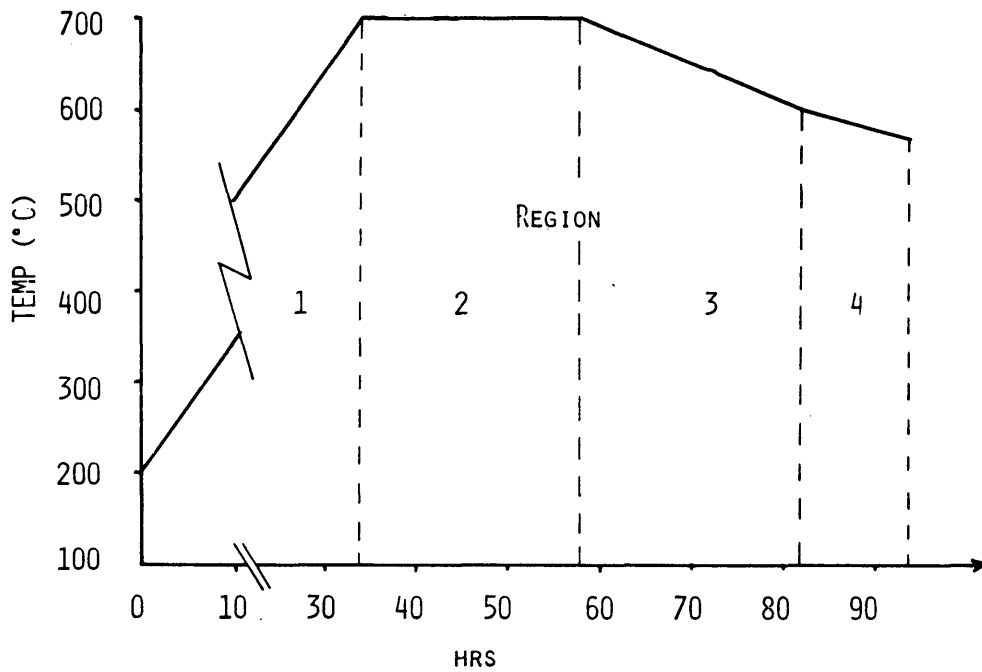


Figure 2.4 Sample heating profile and process program.

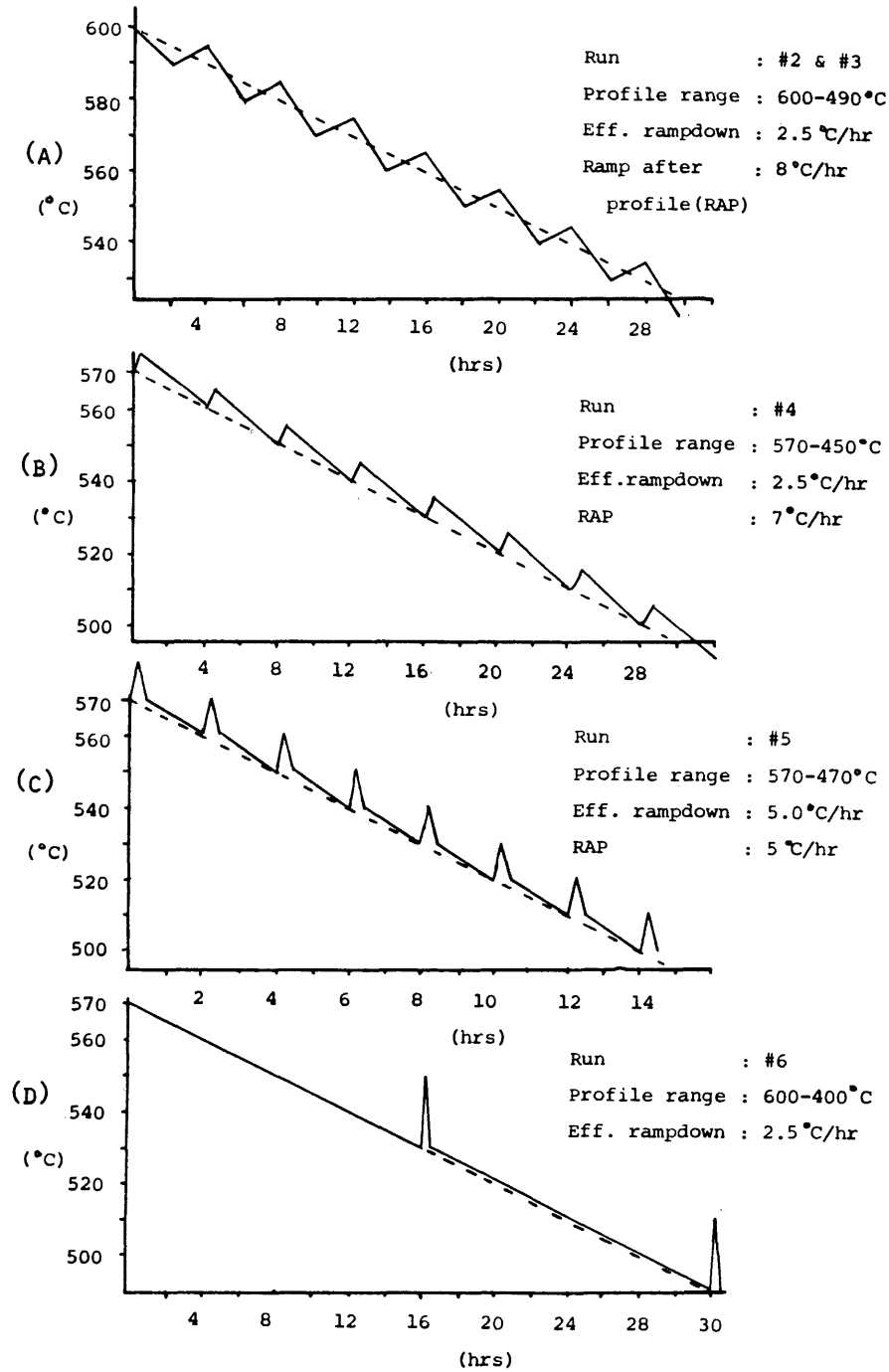
| REGION | FUNCTION | TEMP(°C) | TIME(HR) | RATE(°c/HR) |
|--------|----------|----------|----------|-------------|
| 1 | RAMP(TO) | 700 | 34 | 14.7 |
| 2 | SOAK | 700 | 24 | -- |
| 3 | RAMP | 600 | 24 | -4.1 |
| 4 | RAMP | 570 | 12 | -2.5 |

most effective. From 400°C to 200°C, the sample is cooled at 25°C/hr to below the freezing point of tin (232°C).

Several different cooling profile techniques and effective rampdown rates were employed for runs two through six. They are shown in Figure 2.5. The effective rampdown rate is defined here as the total temperature difference, 570°C - 400°C = 170°C, divided by the total elapsed time between the two temperatures. It is believed that the longer the cooling process, the larger the single crystals will be.

Following the temperature profiling and cooling to room temperature, the ingot is placed in a small beaker, which is placed in a larger beaker of hot glycerin, $T \approx 260^\circ\text{C}$. As the tin melts, the crystals can be withdrawn. Residual tin, which resides on the surface and inside any inclusions that may exist, is etched away in a solution of 4H₂O:3HNO₃:HF for 10-20 minutes. An etchant without HF was tried but tin precipitates deposited on the surface and deteriorated the crystal performance.

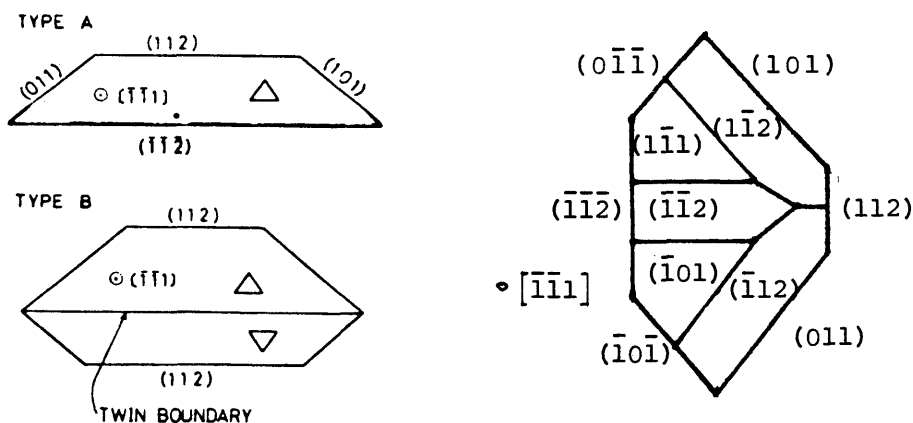
Figure 2.5 Cooling profiles.



2.3 Results & Discussion

The crystal yields are summarized in Table 2.1 for runs #2-6. Included in the table are the conditions under which the run was made, i.e., temperature profiling parameters, heat sink parameters, etc.

The crystals yielded consisted primarily of CdSnP_2 single and poly-crystals with open inclusions and a few Sn_4P_3 plate-like attachments. Residual copper in doped samples dissolved in the tin etchant and plated out on the crystals. It was easily removed with concentrated HNO_3 . The sizes and morphologies ranged from needle-like with $.1 \times .1 \text{ mm}^2$ cross-sections to plate-like with $5.0 \times 1.0 \text{ mm}^2$ cross-sections. Two typical cross-sections are shown below (10,11).



The tin etchant employed did not etch any crystal faces within the time period required to dissolve the excess tin (10-20 min). Surface etching will occur, however, for time periods in the range 2-3 hr (12).

Two cooling techniques were employed. It was originally believed that a "sawtooth" cooling profile would prove to be most effective. Such a profile was used in runs #2, 3, and 4, as shown in Figure 2.5 (a) and (b). However, after the initial temperature rise, the rampdown rate was slow enough to allow the sample to reach thermal equilibrium, thus negating the purpose of the sawtooth profile.

For runs #5 and 6, a spiking technique was employed. A typical profile is shown in Figure 2.5 (c) and (d). With a "spike" period of only 30 minutes, it is likely that only the small crystals will react to the change in temperature and dissolve. As the temperature returns to the pre-spike value, the dissolved CdSnP_2 has the opportunity to recrystallize on an existing crystal site. After the spike is completed, a slow rampdown continues until the next cycle.

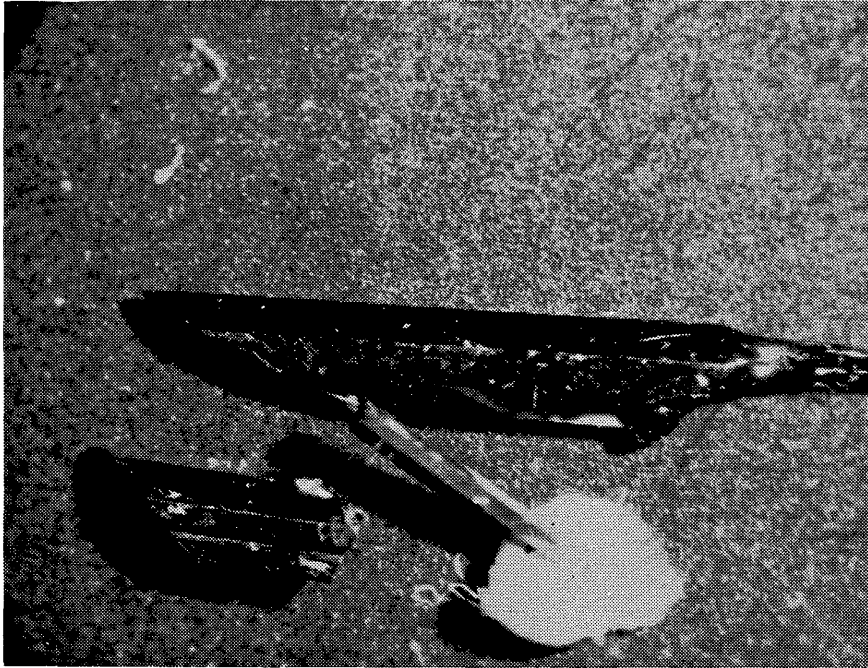
The desired effect on the crystal yield of the cooling profile are not, unfortunately, seen in run #5 due to the detrimental effects of the heat sink method employed. The yield was poly-crystalline in nature. However, positive results were observed in run #6. The spike amplitude was at 20°C , and significantly larger crystals were seen. The morphology of the crystals was layered or stacked, with

open inclusions prevalent, as if one crystal face seeded the growth of a second crystal.

The effect of heat sinks on the crystal yield were clearly dramatic. Nucleation took place preferentially at spots on the ampoule surface where contact was made with either the furnace floor or a block-support. For example, the sample end of the ampoule in run #5 was placed in contact with a block that was formed so as to have good contact with the ampoule surface. The resultant yield consisted of one solid polycrystalline mass in the shape of the ampoule surface! It was virtually impossible to use this sample for characterization studies.

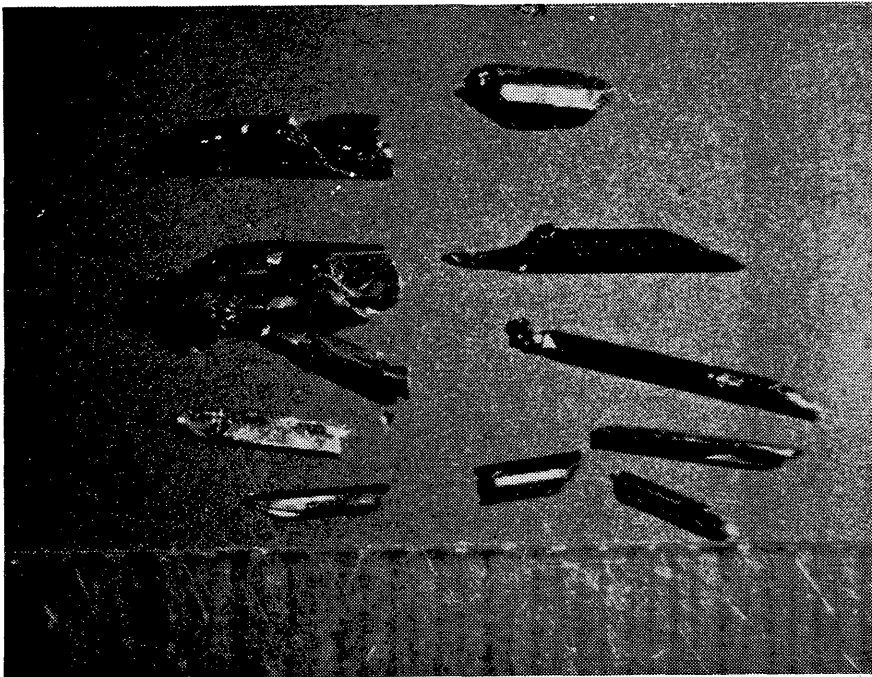
It can be concluded, therefore, that limited control of crystal nucleation sites and crystal size can be realized with appropriate temperature profiling. However, whether this control can produce large single crystals is not yet known. The methods employed in this study were fairly crude. Better control of temperature gradients produced by heat sinks is necessary. Possibly an array of closely spaced thermal conducting probes in contact with the sample reservoir would produce the optimum density of surface nucleation sites. Likewise, a detailed study of the dissolution/crystallization hysteresis effect will lend insight into the optimum shape for the temperature spike.

The electronic properties of the crystals and their relationship with growth technique is discussed in section 4. Several photographs of resultant crystals are shown in Figure 2.6.



10X

Figure 2.6 Photographs of CdSnP₂ crystals.



4X

3. STRUCTURAL CHARACTERIZATION

The chalcopyrite structure of CdSnP_2 is an important factor in determining its characteristic properties, electronic and otherwise. Though the emphasis of this study is not to experimentally investigate or verify many of these structural properties, it is necessary to understand and apply the knowledge to the characterization studies made here. The emphasis of this structural characterization is to verify that our crystal yield includes CdSnP_2 , and to identify other precipitates present, using XRD and to investigate the role of tin in the crystal structure by ^{119}Sn MES.

3.1 General Properties of Chalcopyrites

The chalcopyrite structure of CdSnP_2 possesses the tetragonal EL_1 structure with space group $I\bar{4}2d$, with four formula units per cell. Each Cd and Sn atom is tetragonally coordinated to four P atoms, while each P atom is tetragonally coordinated to two Cd and two Sn atoms. The tetragonal chalcopyrite structure is illustrated in Figure 3.1, alongside its binary analog InP, with its cubic zinc-blende structure.

The distribution of atoms in the unit cell are as follows (13);

Equivalent positions: $(000; \frac{1}{2}, \frac{1}{2}, \frac{1}{2})$

4 Cd in (a) positions, $000; \frac{1}{2}0\frac{1}{4}$

4 Sn in (b) positions, $00\frac{1}{2}; \frac{1}{2}0\frac{3}{4}$

8 P in (d) positions, $X, \frac{1}{4} \frac{1}{8}, \bar{X} \frac{3}{4} \frac{1}{8}, \frac{3}{4} X \frac{7}{8}, \frac{1}{4} \bar{X} \frac{7}{8}$

$$X = .2621$$

These atomic positions are verified through structure factor calculations and observed XRD data.

The tetragonal structure is characterized as a bravais lattice generated by three mutually perpendicular primitive vectors, two of which are of equal length. The length of

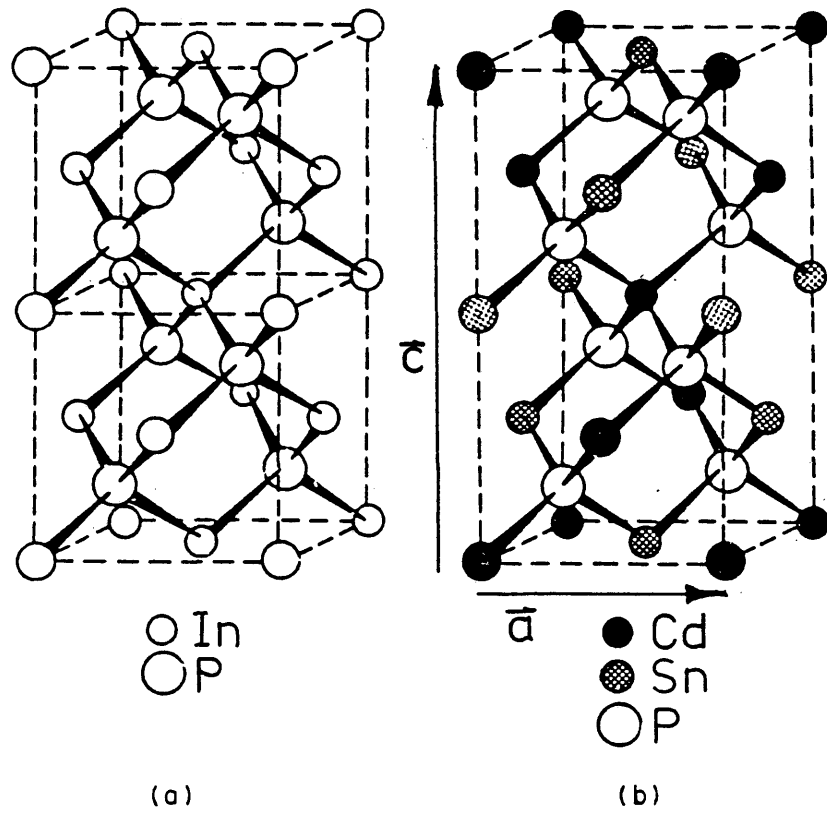


Figure 3.1 The tetragonal chalcopyrite structure illustrated for the II-IV-V₂ compounds. Two cubic zincblende structures are illustrated on the left. (Shay et al, 1971)

these base primitive vectors is denoted by "a". The third axis is called the c-axis and the length of the unit cell along this direction is denoted by "c". Their values, as determined by XRD in this study and others, are: $a = 5.900 \text{ \AA}$ and $c = 11.513 \text{ \AA}$.

If the cations, Sn and Cd, are both replaced by In, the cubic zincblende structure would result (Figure 3.1). Therefore, the chalcopyrite structure is a superlattice of the zinc-blende structure with c/a approximately equal to 2. The tetragonal coordination implies that the Cd-P and Sn-P bonds are primarily covalent with sp^3 hybrid bonds prevalent (14). This will be verified, in part, by MES.

The quantity $[c/a-2]$ is a measure of the tetragonal distortion along the c-axis. For CdSnP_2 , $2-c/a \approx .048$ (15), which is greater than zero and thus indicates, for $X > .25$, a motion of the P atom toward the Sn atom and away from the Cd atom.

One can use this information on atomic positions in the unit cell and tetragonal lattice dimensions, through the structure factor, to predict and calculate allowed x-ray d-spacings and compare the results with experimental and published values.

3.2 X-Ray Diffraction

The crystal growth technique employed in this study involves non-stoichiometric amounts of constituent elements. Consequently, as pointed out earlier, there are several crystal precipitates that derive from the original charge, and they must be identified. We know such possibilities, based upon the CdP₂-Sn phase diagram and probable stoichiometries of constituent elements, to include CdSnP₂, CdP₂, CdP₄, and Sn₄P₃.

X-ray diffraction results for a particular unknown are compared with known d-spacings for suspected crystals as tabulated by the Joint Committee on Powder Diffraction Standards, and thus identified. The main purpose of this identification process is to qualitatively determine the effectiveness of the growth technique by identifying non-CdSnP₂ precipitates and consequently minimizing their yield through changes in stoichiometry or temperature profiling. Thus far, it has been our experience that Sn₄P₃ is the most common undesired precipitate.

3.2.1 XRD Theory

Typical interatomic distances in a solid are on the order of 10^{-8} cm. To probe these distances, electromagnetic radiation of wavelengths no longer than these characteristic lengths must be used. Wavelengths on the order of 10^{-8} cm are characteristic of x-rays. The distribution of x-rays scattered by a rigid periodic array of ions reveals the locations of the ions within the structure. This study incorporates the Bragg formulation of x-ray diffraction by a crystal.

A crystal can be regarded as made out of a family of crystal planes of ions, spaced a distance d -apart. There are two necessary conditions for a sharp peak in the intensity of scattered radiation: 1) that the x-rays be specularly reflected by the ions in any one plane and 2) that the reflected rays from successive planes interfere constructively. The path difference between such rays is $2d\sin\theta$, where θ is the angle of incidence. The condition for constructive interference leads to the Bragg condition

$$n\lambda = 2d\sin\theta. \quad (3.1)$$

The integer n is known as the order of the corresponding reflection and principal diffraction peaks occur for $n = 1$. λ is the wavelength of the incident x-ray radiation. Typically, the radiation is produced by relaxation

transitions in crystals such as copper. There will usually exist two principle transitions producing α_1 and α_2 x-rays with only slightly different wavelengths. This, in turn, will produce two diffraction peaks. However, they are only resolvable at higher angles. Where a single peak exists (small θ), a weighted average of λ_{α_1} and λ_{α_2} is used in d-space calculations.

A well known theorem states that for any reciprocal lattice vector \vec{k} , there is a family of lattice planes normal to \vec{k} and separated by a distance d , where $2\pi/d$ is the length of the shortest reciprocal lattice vector parallel to \vec{k} :

$$|\vec{k}| = \frac{2\pi n}{d} \quad (3.2)$$

Solving for d in 3.1 and plugging into 3.2 yields the relation

$$\sin\theta = \frac{\lambda}{4\pi} |\vec{k}| \quad (3.3)$$

For a tetragonal unit cell of dimensions $a \times a \times c$ Å, the reciprocal lattice vector is given by

$$\vec{k} = 2\pi \left(\frac{h\hat{x}}{a} + \frac{k\hat{y}}{a} + \frac{l\hat{z}}{c} \right) \quad (3.4)$$

where (hkl) are the Miller indices of the real lattice plane of reflection, and are the coordinates of the shortest reciprocal lattice vector normal to that plane.

Substituting eqn. 3.4 into 3.3, and squaring

$$\sin^2\theta = (h^2 + k^2)A + l^2C$$

with

$$A = \frac{\lambda^2}{4a^2} \text{ and } C = \frac{\lambda^2}{4c^2} \quad (3.5)$$

Equation 3.5 allows us to calculate, from experimental data ($\sin\theta$), and the (hkl) value for that diffraction peak, the lattice parameters a and c. However, determining the allowed (hkl) is a formidable problem. They are primarily dependent on the structure of the unit cell, i.e., tetragonal, hexagonal, etc., as is the actual form of Eqn. 3.5. Were we starting from first principles, we could calculate the allowed (hkl) values for each lattice type by trial and error match them to observed θ -values, and determine whether consistent values for the lattice parameters can be calculated. For the purpose of this study, we begin with the knowledge that the unit cell of CdSnP_2 is tetragonal. To calculate the allowed (hkl) for observed diffraction peak maxima, we turn to the geometrical structure factor.

The CdSnP_2 crystal structure consists of a polyatomic lattice with a 16-atom basis. The structure can further be broken into three interlocking monatomic lattices with an n-atom basis: $n = 4$ for Cd and Sn fcc sublattices and $n = 8$ for the P diamond sublattice. Within each sublattice exists identical scattering positions $d_1 \dots d_n$, as listed earlier as equivalent positions. The intensity of

radiation in a given Bragg peak depends on the extent to which the rays scattered from these sublattices interfere with one another. The scattering intensity per sublattice is weighted by their atomic form factor, $f(\vec{k})$, which is related to the scattering power of the atom and is proportional to the number of electrons associated with that atom in the crystal structure. The net ray scattered by the entire unit cell is the sum of the individual rays, with the proper weighting, and has an amplitude containing the factor

$$S(\vec{k}) = \sum_{\alpha=1}^3 f_{\alpha} \sum_{j=1}^n e^{i(\vec{\kappa} \cdot \vec{d}_j)_{\alpha}} \quad (3.6)$$

For any combination of (hkl) that produces $S(\vec{k}) \neq 0$, there exists a non-zero diffraction peak. Conversely, if $S(\vec{k})$ is very small, the respective (hkl) indices indicate a crystal plane from which Bragg reflections cannot occur. In general, the f_{α} 's are different for each constituent atom, and dependent on scattering direction. We are, therefore, lead to believe that the only probable means of obtaining a zero sum is if the sum for each atom alone is zero. However, we find that such a condition rarely occurs. In actuality, the form factor for each atom depends on the ionic character of each atom in the

structure. We have several times mentioned the analogy between CdSnP_2 and InP . The Cd, valence II, and Sn, valence IV, atoms combine to establish an electronic structure very similar to In, valence III, such that the net effective charge on each is equivalent to that on In. The form factors for Cd and Sn are, therefore, approximately equal. For the purpose of the calculations to follow (Appendix 1), we will normalize f_{Cd} and f_{Sn} to one. The relative value of f_{P} is approximately equal to the ratio of the total number of electrons of P to Cd^{-1} , or Sn^{+1} , that is $15/50 \approx .30$.

The derivation of the structure factor is given in Appendix 1. The results are summarized in Table 3.1. We see that the calculated (hkl) correspond exactly to the known values seen in Figure 3.2. It seems that a few (hkl) appear as allowed planes that do not appear in JCPDS data, and have equivalent d-spacings as (khl) indices. This is a property of the $I\bar{4}2d$ (D_{2d}^{12}) space group and is seen in the symmetry of the Cd and Sn sites in the tetragonal chalcopyrite structure.

The calculated d-spacing values (eqn. 3.2), incorporating the known lattice parameters a and c, also exhibit very good agreement with known values seen in Figure 3.2. In turn, the theory is also supported by

Table 3.1 Structure Factor Results for CdSnP₂

| R | K | L | S(CI) | S(SN) | S(F) | S(TOI) | AMP | I (Å) |
|---|---|----|--------------|--------------|--------------|---------|--------|-------|
| 1 | 1 | 2 | 4.00+I 0.00 | 4.00+I 0.00 | 0.00+I 7.96 | 8.00+I | 69.73 | 3.378 |
| 2 | 0 | 0 | 4.00+I 0.00 | 4.00+I 0.00 | -7.95+I 0.00 | 5.61+I | 31.52 | 2.950 |
| 0 | 2 | 4 | 4.00+I 0.00 | 4.00+I 0.00 | -6.00+I 0.00 | 5.60+I | 31.36 | 2.878 |
| 2 | 2 | 0 | 4.00+I 0.00 | 4.00+I 0.00 | 7.91+I 0.00 | 10.37+I | 107.58 | 2.056 |
| 2 | 0 | 4 | 4.00+I 0.00 | 4.00+I 0.00 | 7.95+I 0.00 | 10.35+I | 107.87 | 2.000 |
| 0 | 2 | 4 | 4.00+I 0.00 | 4.00+I 0.00 | 7.95+I 0.00 | 10.39+I | 107.87 | 2.000 |
| 0 | 2 | 1 | 2.00+I -2.00 | -2.00+I 2.00 | -0.21+I 0.21 | -0.00+I | 0.00 | 0.00 |
| 3 | 1 | 2 | 4.00+I 0.00 | 4.00+I 0.00 | 0.00+I -7.98 | 8.00+I | 69.60 | 1.775 |
| 1 | 1 | 0 | 4.00+I 0.00 | 4.00+I 0.00 | 0.00+I -7.98 | 8.00+I | 69.73 | 1.743 |
| 2 | 4 | 4 | 4.00+I 0.00 | 4.00+I 0.00 | -7.91+I 0.00 | 5.63+I | 31.07 | 1.669 |
| 4 | 0 | 0 | 4.00+I 0.00 | 4.00+I 0.00 | 7.82+I 0.00 | 10.34+I | 107.02 | 1.475 |
| 0 | 0 | 0 | 4.00+I 0.00 | 4.00+I 0.00 | 6.00+I 0.00 | 10.40+I | 106.16 | 1.435 |
| 3 | 3 | 2 | 4.00+I 0.00 | 4.00+I 0.00 | 0.00+I 7.79 | 8.00+I | 69.47 | 1.352 |
| 3 | 1 | 0 | 4.00+I 0.00 | 4.00+I 0.00 | 0.00+I 7.68 | 8.00+I | 69.60 | 1.338 |
| 4 | 2 | 0 | 4.00+I 0.00 | 4.00+I 0.00 | -7.77+I 0.00 | 5.67+I | 32.14 | 1.319 |
| 4 | 0 | 4 | 4.00+I 0.00 | 4.00+I 0.00 | -7.82+I 0.00 | 5.64+I | 31.98 | 1.313 |
| 0 | 0 | 0 | 4.00+I 0.00 | 4.00+I 0.00 | -7.95+I 0.00 | 5.61+I | 31.52 | 1.293 |
| 4 | 2 | 4 | 4.00+I 0.00 | 4.00+I 0.00 | 7.77+I 0.00 | 10.33+I | 106.73 | 1.199 |
| 2 | 2 | 4 | 4.00+I 0.00 | 4.00+I 0.00 | 7.91+I 0.00 | 10.37+I | 107.58 | 1.185 |
| 5 | 1 | 2 | 4.00+I 0.00 | 4.00+I 0.00 | 0.00+I 7.70 | 8.00+I | 69.34 | 1.134 |
| 3 | 3 | 6 | 4.00+I 0.00 | 4.00+I 0.00 | 0.00+I -7.79 | 8.00+I | 69.47 | 1.126 |
| 1 | 1 | 10 | 4.00+I 0.00 | 4.00+I 0.00 | 0.00+I 7.98 | 8.00+I | 69.73 | 1.110 |
| 4 | 4 | 0 | 4.00+I 0.00 | 4.00+I 0.00 | 7.63+I 0.00 | 10.29+I | 105.68 | 1.043 |
| 4 | 0 | 0 | 4.00+I 0.00 | 4.00+I 0.00 | 7.82+I 0.00 | 10.35+I | 107.02 | 1.030 |
| 5 | 3 | 3 | 4.00+I 0.00 | 4.00+I 0.00 | 0.00+I -7.61 | 8.00+I | 69.21 | 0.997 |
| 0 | 4 | 2 | 0.00+I 0.00 | 0.00+I 0.00 | 0.00+I 0.23 | 0.00+I | 0.00 | 0.00 |
| 5 | 1 | 6 | 4.00+I 0.00 | 4.00+I 0.00 | 0.00+I -7.70 | 8.00+I | 69.34 | 0.991 |
| 3 | 1 | 10 | 4.00+I 0.00 | 4.00+I 0.00 | 0.00+I -7.70 | 8.00+I | 69.60 | 0.980 |
| 4 | 2 | 8 | 4.00+I 0.00 | 4.00+I 0.00 | -7.77+I 0.00 | 5.67+I | 32.14 | 0.972 |
| 6 | 2 | 0 | 4.00+I 0.00 | 4.00+I 0.00 | 7.54+I 0.00 | 10.26+I | 105.34 | 0.933 |
| 0 | 0 | 4 | 4.00+I 0.00 | 4.00+I 0.00 | 7.59+I 0.00 | 10.28+I | 105.62 | 0.931 |
| 2 | 0 | 12 | 4.00+I 0.00 | 4.00+I 0.00 | 7.95+I 0.00 | 10.39+I | 107.87 | 0.912 |
| 5 | 3 | 6 | 4.00+I 0.00 | 4.00+I 0.00 | 0.00+I 7.61 | 8.00+I | 69.21 | 0.895 |
| 0 | 2 | 4 | 4.00+I 0.00 | 4.00+I 0.00 | -7.54+I 0.00 | 5.74+I | 32.91 | 0.887 |
| 3 | 3 | 10 | 4.00+I 0.00 | 4.00+I 0.00 | 0.00+I 7.75 | 8.00+I | 69.47 | 0.887 |
| 2 | 2 | 12 | 4.00+I 0.00 | 4.00+I 0.00 | -7.91+I 0.00 | 5.63+I | 31.67 | 0.872 |
| 4 | 4 | 8 | 4.00+I 0.00 | 4.00+I 0.00 | 7.63+I 0.00 | 10.29+I | 105.68 | 0.845 |
| 7 | 1 | 2 | 4.00+I 0.00 | 4.00+I 0.00 | 0.00+I -7.44 | 8.00+I | 66.96 | 0.838 |
| 5 | 1 | 10 | 4.00+I 0.00 | 4.00+I 0.00 | 0.00+I 7.70 | 8.00+I | 69.34 | 0.816 |
| 0 | 0 | 0 | 4.00+I 0.00 | 4.00+I 0.00 | -7.55+I 0.00 | 5.72+I | 32.75 | 0.812 |
| 1 | 1 | 14 | 4.00+I 0.00 | 4.00+I 0.00 | 0.00+I -7.98 | 8.00+I | 69.73 | 0.807 |
| 6 | 4 | 4 | 4.00+I 0.00 | 4.00+I 0.00 | 7.41+I 0.00 | 10.22+I | 104.49 | 0.787 |
| 0 | 2 | 0 | 4.00+I 0.00 | 4.00+I 0.00 | 7.54+I 0.00 | 10.26+I | 105.34 | 0.783 |
| 4 | 2 | 12 | 4.00+I 0.00 | 4.00+I 0.00 | 7.77+I 0.00 | 10.33+I | 106.73 | 0.776 |

22-517

| d | | 3.38 | 2.06 | 1.77 | 3.38 | CdSnP ₂ | | | | |
|-------------------|--|----------------|-----------------------|----------|-------|-----------------------|-------|-------|------------------|-----------|
| 1/1 ₁ | | 100 | 55 | 50 | 100 | Cadmium Tin Phosphide | | | | |
| Rad. | CuKα ₁ λ | 1.5405 | Filter | Ni | Dia. | 114.6mm | | | | |
| Cur off | 1/1 ₁ Photometer | | | | | | | | | |
| Ref. | Smith, The Plessey Company Limited, Allen Clark Research Centre, Caswell, Towcester, Northants, U.K. | | | | | | | | | |
| Sys. | Tetragonal S.G. 142d (122) | | | | | | | | | |
| a ₀ | 5.900 | b ₀ | c ₀ 11.513 | | A | C | 1.951 | | | |
| a | β | | γ | Z | 4 | Dx | 4.85 | | | |
| Ref. | Ibid. | | | | | | | | | |
| εα | | | | | | | | | | |
| 2V | D | nωβ | mp | εγ | Color | Sign | | | | |
| Ref. | | | | | | | | | | |
| Chalcopyrite type | | | | | | | | | | |
| | | d Å | 1/1 ₁ | hkl | d Å | 1/1 ₁ | hkl | d Å | 1/1 ₁ | hkl |
| | | 3.38 | 100 | 112 | 1.028 | 4 | 408 | 0.995 | 6 | 532 |
| | | 2.88 | 8 | 004 | .989 | 8 | 516 | .978 | 8 | 310 |
| | | 2.09 | 20 | 220 | .972 | 4 | 428 | .932 | 6 | 620 |
| | | 2.06 | 55 | 204 | .930 | 6 | 604 | .912 | 6 | 2012 |
| | | 1.77 | 50 | 312 | .894 | 8 | 536 | .887 | 8 | 624, 3310 |
| | | 1.74 | 18 | 116 | .872 | 2 | 2212 | .844 | 8 | 448 |
| | | 1.69 | 8 | 224 | .826 | 12 | 712 | .8159 | 10 | 5110 |
| | | 1.47 | 6 | 400 | .8115 | 2 | 608 | .8063 | 6 | 1114 |
| | | 1.44 | 2 | 008 | .7870 | 25 | 644 | .7829 | 20 | 628 |
| | | 1.35 | 8 | 332 | .7760 | 30 | 4212 | | | |
| | | 1.34 | 14 | 316 | | | | | | |
| | | 1.315 | 10 | 420, 404 | | | | | | |
| | | 1.290 | 4 | 208 | | | | | | |
| | | 1.197 | 16 | 424 | | | | | | |
| | | 1.182 | 8 | 228 | | | | | | |
| | | 1.133 | 8 | 512 | | | | | | |
| | | 1.124 | 4 | 336 | | | | | | |
| | | 1.108 | 4 | 1110 | | | | | | |
| | | 1.041 | 4 | 440 | | | | | | |

Joint Committee on Powder Diffraction Standards 1972

Figure 3.2 CdSnP₂ d-spacings (16)

experimental results, within experimental error, as shown in the next section.

3.2.2 Experimental Procedure

All material to be analyzed was ground into a fine powder and mounted on a glass slide with double stick tape. Samples from Runs #2 and #6 were analyzed. The slide was placed in the goniometer of the Rigaku D/MAX Automated X-Ray Diffraction System. The data accumulation was controlled by the Control/Data Processing unit terminal. A sample program was shown below. The count rate determines full scale setting of the chart recorder while the time constant relates to the detector response and scan rate. A typical x-ray power is 1600 W (40 kV @ 40 mA).

Results are seen on a chart recorder with X-corresponding to 2θ and Y corresponding to count rate.

```
Sample Program: Mode: Continuous Scan
                Drive Axis: 2 $\theta$ / $\theta$ 
                Scan Range: 20°-100°
                Scan Speed: 1 deg/min
                Count rate: 10K counts/sec
Time Constant: 2 sec
                Chart speed: 10 mm/min
```

3.2.3 Results

XRD data showing diffraction peaks for a crystal from run #6 are shown in Figure 3.3. Table 3.2 includes corresponding d-spacings and (hkl) values for each diffraction peak. Lattice parameters a and c were calculated from a least squares fit to eqn. 3.5, and are

$$a = 5.904 \pm .006 \text{ \AA} \text{ and } c = 11.513 \pm .002 \text{ \AA}$$

These values are in good agreement with JCPDS values noted earlier. With agreement between structure factor calculations and experiment, it can be concluded that the structure of CdSnP_2 is the tetrahedrally coordinated chalcopyrite structure introduced.

Further XRD studies indicate the presence of Sn_4P_3 platelets in our crystal yields. The material formed at the top of the ampoule in run #1 by vapor transport is CdP_4 . We did not, however, detect the presence of CdP_2 in any yield, thus substantiating our desired position on the CdP_2 -Sn phase diagram.

Figure 3.3 XRD results of CdSnP₂.

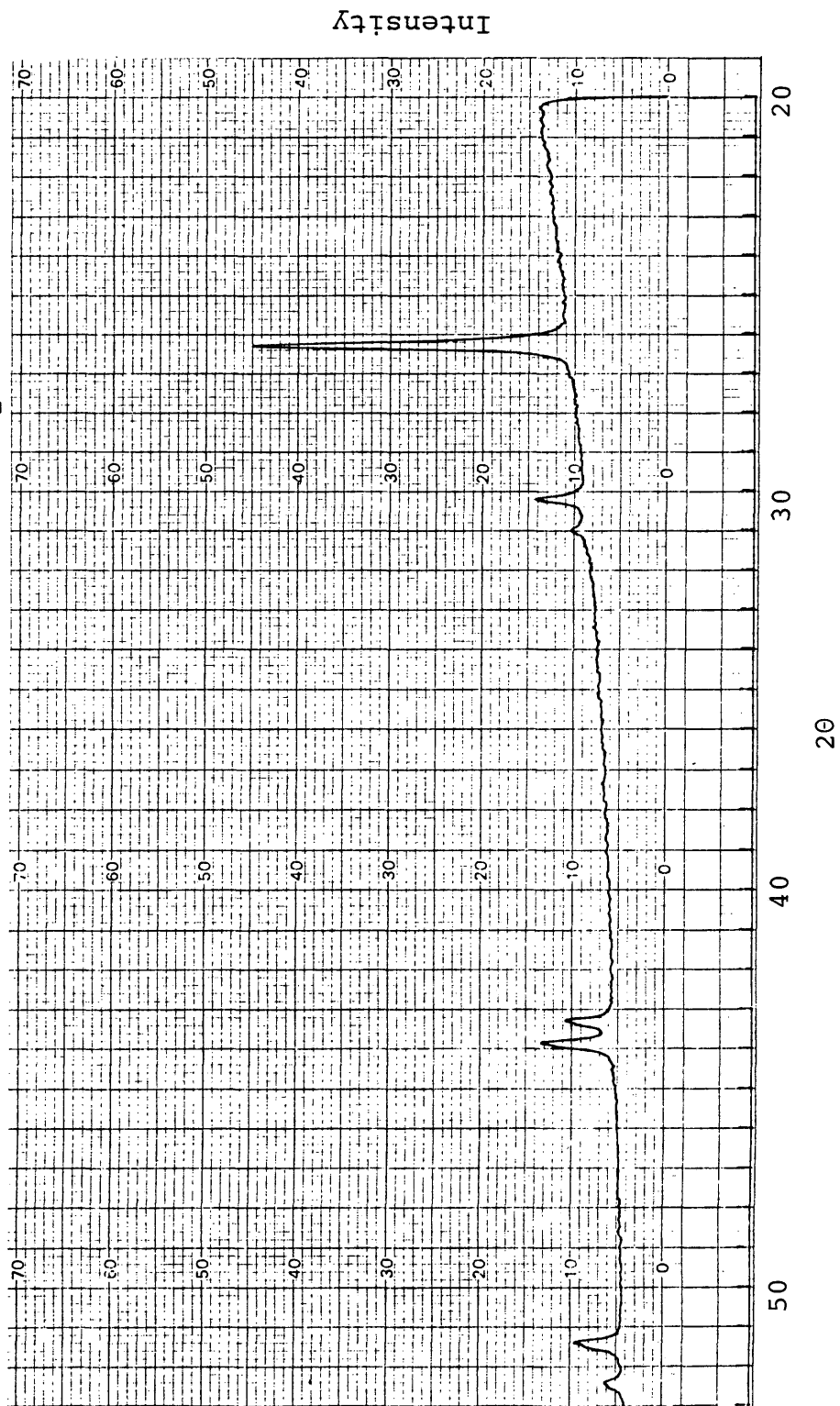


Table 3.2 D-spacing and Lattice Parameter
Calculations From XRD Data

$$\text{SIN}^2\theta = (H^2+K^2)A + L^2C ; A = \lambda_{av}^2/4a^2 ; C = \lambda_{av}^2/4c^2$$

$$\lambda_{\alpha_1} = 1.5405 \text{ \AA} ; \lambda_{av} = 1/3(2\lambda_{\alpha_1} + \lambda_{\alpha_2})$$

$$\lambda_{\alpha_2} = 1.5443 \text{ \AA} = 1.5418 \text{ \AA}$$

$$\Delta\theta = \pm .1^\circ \quad \Delta D = -D/\text{TAN}\theta \times \Delta\theta, \quad |\Delta D| < .010$$

| 2 θ | SIN θ | D(\AA) | SIN ² θ | HKL |
|------------|--------------|-------------------|---------------------------|-----|
| 26.30 | .2275 | 3.388 | .0517 | 112 |
| 30.20 | .2605 | 2.959 | .0678 | 200 |
| 30.90 | .2663 | 2.893 | .0709 | 004 |
| 43.30 | .3689 | 2.089 | .1362 | 220 |
| 43.90 | .3737 | 2.062 | .1396 | 204 |
| 51.45 | .4341 | 1.776 | .1883 | 312 |
| 52.45 | .4418 | 1.744 | .1951 | 116 |
| 54.30 | .4563 | 1.689 | .2082 | 224 |
| 63.00 | .5224 | 1.475 | .2729 | 400 |
| 64.70 | .5351 | 1.440 | .2862 | 008 |
| 69.50 | .5699 | 1.352 | .3247 | 332 |
| 70.40 | .5764 | 1.337 | .3322 | 316 |
| 80.00 | .6427 | 1.199 | .4130 | 404 |

$$A = 1.7047 \pm .0036 \times 10^{-2} \Rightarrow a = 5.9043 \pm .0062 \text{ \AA}$$

$$C = 4.483 \pm .0012 \times 10^{-3} \Rightarrow c = 11.513 \pm .0015 \text{ \AA}$$

3.3 Mössbauer Effect Spectroscopy

Mössbauer Effect Spectroscopy (MES) is a diverse tool that can lend insight into many different scientific fields of study, including solid state research. In particular, this study is interested in extracting information on chemical bonding and crystal structure from the electric interactions reflected in the Mössbauer spectra. We are able to conduct this study because CdSnP_2 contains ^{119}Sn , a Mössbauer active element. Our results will substantiate the proposition that the Sn sublattice exhibits tetragonal coordination with an atomic electron structure based upon sp^3 hybrid bonds, as well as show that our CdSnP_2 crystals contain a small percentage of an undesired precipitate, Sn_4P_3 .

3.3.1 Theory

The major measurements available in Mössbauer studies involve the interaction of the nucleus with the electric and magnetic fields in which it is immersed. Three effects related to this interaction include: 1) magnetic dipole interaction, 2) electronic quadrupole interaction, and 3) isomeric monopole interaction. Our studies of the Mössbauer effect in CdSnP_2 will draw primarily on the existence of the isomeric monopole interaction, which produces a characteristic isomer shift for the material under study, and the absence of any electric quadrupole interactions.

The isomeric monopole interaction is a consequence of two fundamental properties of nuclear and atomic structures. Firstly, γ -ray emission and absorption within the tin nucleus possess a certain probability of being recoilless. Secondly, due to the finite size of the nucleus there exists an interaction energy between the valence electron levels with zero, or near zero, angular momentum and the nuclear core potential. When a transition occurs between nuclear levels, energies on the order of tens of kilovolts are liberated in the form of characteristic γ -rays. The nuclear radii will be different for the states connected by the resonant gamma transition.

The gamma ray energy of the ^{119}Sn Mössbauer transition can be written as

$$E_\gamma = E_0 - \Delta E_V \quad (3.7)$$

where E_0 is the transition energy of the bare tin nucleus and ΔE_V is the change in coulomb energy due to the change in nuclear volume upon excitation. The value is given by the relation

$$\Delta E_V = \frac{2}{5} \pi Z e^2 \Delta R^2 \rho_e(0) \quad (3.8)$$

where ΔR^2 is the difference of the square of the tin nuclear radius between the ground state and the excited state, and $\rho_e(0)$ is the density of electrons at $r = 0$.

If $\rho_e(0)$ differs between the source(s) and absorber (a), ΔE_V will be different for the source and absorber. Thus, $E_\gamma(a) \neq E_\gamma(s)$, and the resonant condition will not be fulfilled. In order to obtain resonance, the energy of the emitted gamma ray must be shifted by an amount

$$\Delta E = \Delta E_V(a) - \Delta E_V(s) \quad (3.9)$$

This energy shift is achieved by a relative motion of the source and absorber with a Doppler velocity.

$$V = c \Delta E / E_\gamma(s) \quad (3.10)$$

From equations 3.8 and 3.9

$$V = \frac{2}{5} \frac{\pi c}{E_\gamma} Z e^2 \Delta R^2 \Delta \rho_e(0) \quad (3.11)$$

with

$$\Delta \rho_e(0) = [\rho_e(0)]_a - [\rho_e(0)]_s \quad (3.12)$$

V is called the isomer shift, the name reflecting the fact that ΔR^2 refers to two isomeric states of the tin nuclide.

Although ΔR can be calculated, the concept is not well understood by nuclear theorists. However, $\Delta\rho_e(0)$ is a well understood concept and can be approximated from first principles. The ground state electron densities, which are proportional to $|\psi(0)|^2$, are dominated by s-electrons. There exists only a very small contribution from $P_{1/2}$ electrons in high Z cases, a relativistic effect. The 1s electrons contribute some 80%(17) of the total density. Since there is usually a negligible change in the 1s-4s behavior with chemical binding, and the contribution from the large changes in 5s-5p behavior are small, it is reasonable to expect $|\psi_s^2(0) - \psi_a^2(0)|$ is small compared to either alone. The relative difference one finds is on the order of 10^{-4} .

Though there is not a large contribution from other electrons, their presence is felt in terms of shielding of outer s-orbitals.

From equation 3.11 it can be seen that $\Delta\rho_e(0)$ is directly proportional to V, the isomer shift. Since the CaSnO_3 source is a well understood material, $\rho_e(0)$ for the source can be extracted from $\Delta\rho_e(0)$, thus leaving $\rho_e(0)$ for the absorber, CdSnP_2 . The objective from here, for those

working from first principles, is to develop a model for the electron configuration of the absorber using, e.g., the Hartree-Fock self-consistent field method (18) such that a calculation of $\rho_e(0)$ from this model yields the value determined by experiment. Many such calculations for tin have been made and are summarized in (17,18). This study has relied upon such material to make conclusions regarding the electronic structure of Sn in CdSnP₂. Lees and Flinn (1968), for example, have obtained a general result for the isomer shift as a function of effective number of 5s and 5p electrons.

$$V = -.38 + 3.01 n_s - .20 n_s^2 - .17 n_s n_p \quad (3.13)$$

The function is plotted in Figure 3.4. Knowledge of the isomer shifts leads to a reasonable understanding of the electronic structure.

With $\Delta R/R$ on the order of 10^{-4} (19) and $\Delta\rho/\rho$ on the order of 10^{-4} , isomer shift energies on the order of 10^{-7} eV can be expected and are seen, corresponding to Doppler velocities on the order of a few mm/sec.

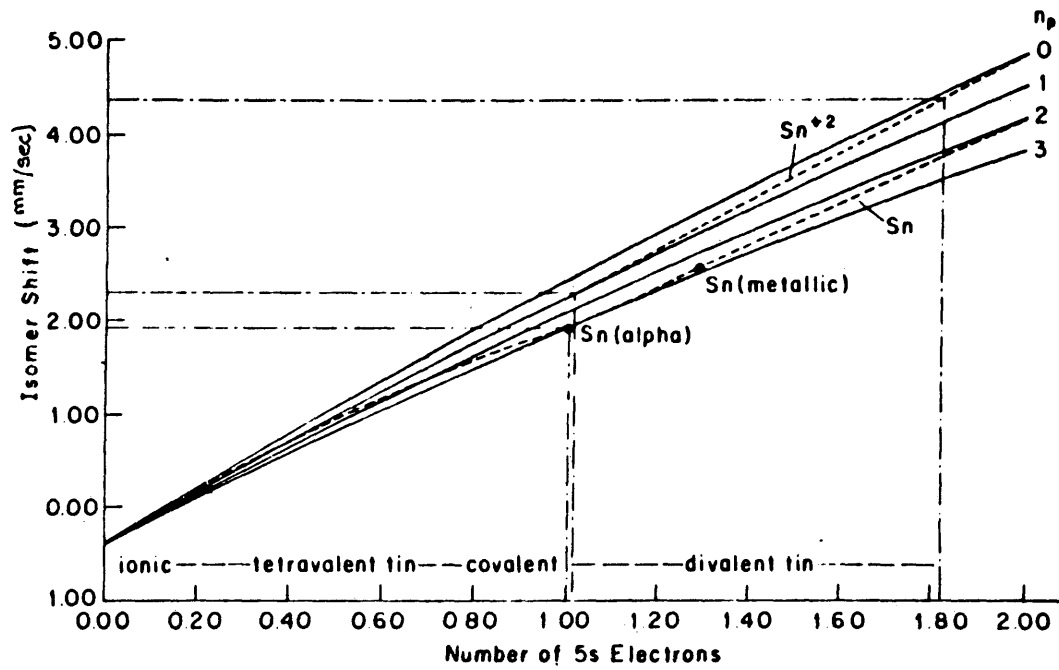


Figure 3.4 Isomer shift as a function of the effective number of 5s and 5p electrons.
(Lees and Flinn, 1968)

3.3.2 Experimental Procedure

20 mg crystal samples were ground into a fine powder and added to 200 mg powdered sugar, mixed, and compressed into 1.3 cm diameter pellets at 3 kpsi in a specimen mount press, and sealed between two adhesive paper disks.

The desired spectra were accumulated using a constant acceleration spectrometer consisting of a multichannel analyzer, a conventional feedback controlled driving unit, and amplifier pulse height analyzer. The radiation source was $\text{CaSnO}_3:^{119}\text{Sn}$.

The 23.8 keV gamma rays were detected with a Xe (CO_2 quenched) gas proportional counter. The velocity calibration was accomplished with a SnTe-CaSnO_3 absorber in order that both a zero and non-zero isomer shift would be seen. The velocity calibration spectrum is shown in Figure 3.5(a). The isomer shift for SnTe absorber is known to be 3.405 mm/sec. Thus, with a channel separation of 71.49 \pm 0.15 channels, the scale is calibrated to be

$$\frac{3.405 \text{ mm/sec}}{71.49 \text{ channels}} = 0.4763 \frac{\text{mm}}{\text{sec-channel}}.$$

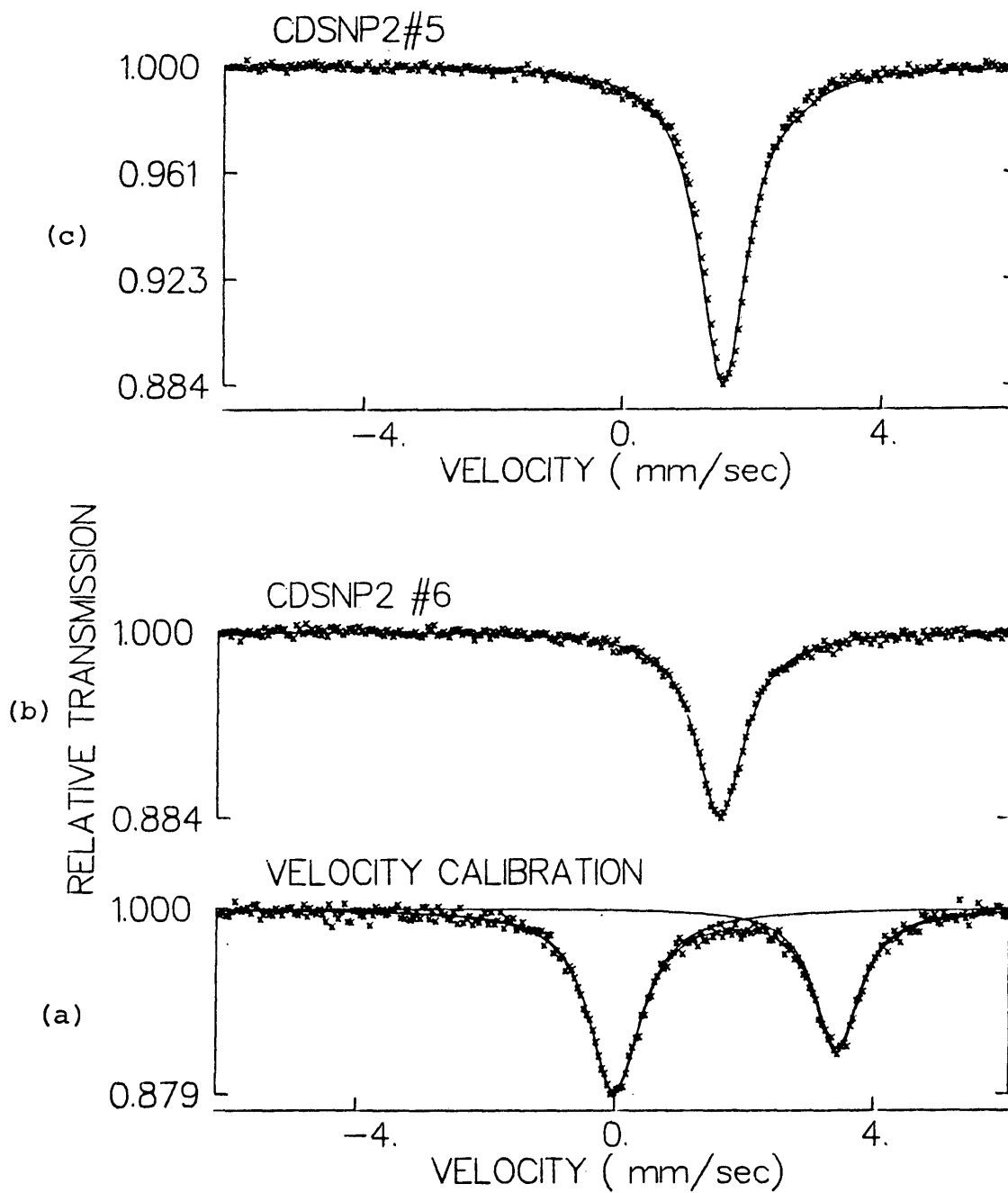


Figure 3.5 Mössbauer Spectra

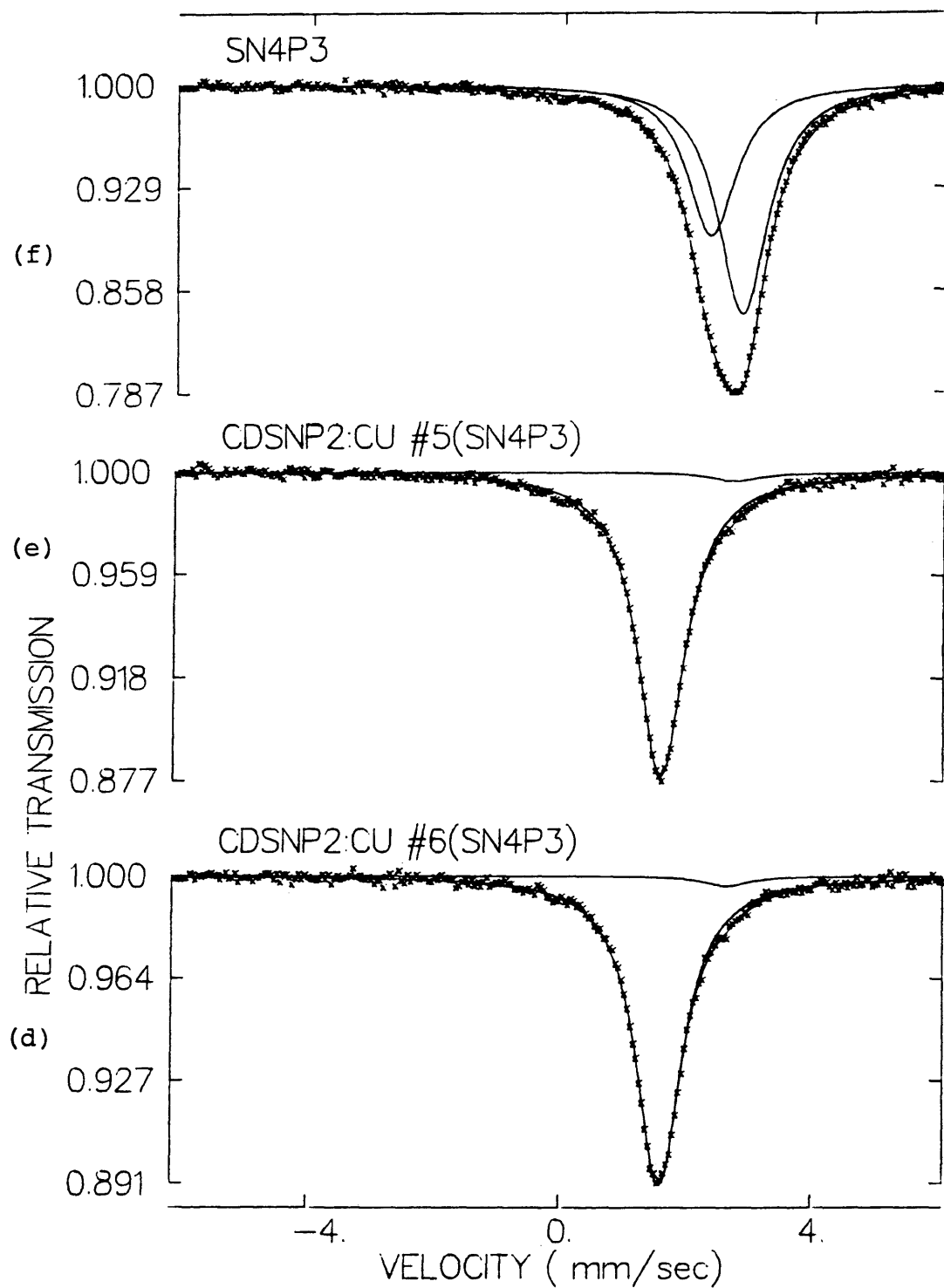


Figure 3.5 Mössbauer Spectra

3.3.3 Results and Disucssion

Five samples were prepared and their Mössbauer spectra analyzed. Additionally, a previous analysis made on a Sn_4P_3 sample is included for comparison. The resultant spectra for the four CdSnP_2 samples and the Sn_4P_3 sample are shown in Figures 3.5(b)-(f). The results are summarized in Table 3.3

Spectra shown here for undoped samples from runs #5 and #6 were essentially identical to the spectra for the 0.1% Cu-doped samples of runs #2 and #3 not shown. It was possible on all three to fit the data to a single lorentzian line centered about channel #161.67 \pm .05, thus giving an average isomer shift, relative to CaSnO_3 source (channel #128.25), of $V = 1.601 \pm 0.002 \frac{\text{mm}}{\text{sec}}$. Chi-squared (χ^2), a measure of the difference between the data and the fitted line, were all less than 1.200, with 1.000 indicating an ideal statistical fit.

However, such was not the case for the 0.5% Cu-doped samples in runs #5 and #6. An attempt to fit the data to a single line yielded a $\chi^2 = 1.324$ and 1.209, respectively. Consequently, a second small absorption peak of equal width was introduced at the position of the Sn_4P_3 isomer shift. The resultant χ^2 were .965 and 1.088 for runs #5 and #6, respectively! The position of the minimum for each

Table 3.3 Mossbauer Spectra Results

Source: CaSnO_3 : ^{119}Sn Calibration: .04792 $\frac{\text{mm}}{\text{sec-channel}}$ δ_0 : 128.25 \pm .10

| Sample | δ :min (Channel #) | $\delta - \delta_0$ | $V = \frac{(\delta - \delta_0)}{(\text{mm/sec})} \times \text{Cal.}$ | χ^2 | $\epsilon \left(\frac{\Delta \text{ counts}}{\text{baseline}} \right) (\%)$ |
|-----------------------|------------------------------|---------------------|--|----------|--|
| CdSnP ₂ #6 | 161.68 \pm .07 | 33.43 | 1.602 \pm .003 | 1.029 | 11.43 |
| #5 | 161.62 \pm .04 | 33.37 | 1.599 \pm .007 | 1.193 | 11.53 |
| :Cu(.1%) #2-#3 | 161.61 \pm .04 | 33.37 | 1.598 \pm .007 | .984 | 11.51 |
| :Cu(.5%) #6 | 161.81 \pm .04 | 33.56 | 1.608 \pm .007 | 1.209 | 10.97 |
| :Cu(.5%) #5 | 161.71 \pm .04 | 33.46 | 1.603 \pm .007 | 1.324 | 12.03 |

| Sample | δ_1 | $\epsilon_1 (\%)$ | $\delta_1 - \delta_0$ | V_1 (mm/sec) | δ_2 | $\epsilon_2 (\%)$ | $\delta_2 - \delta_0$ | V_2 (mm/sec) | χ^2 | ϵ_2 / ϵ_1 |
|--------------------------------------|------------------|-------------------|-----------------------|------------------|-------------------|-------------------|-----------------------|------------------|----------|---------------------------|
| CdSnP ₂ :Cu #6 | 161.67 \pm .04 | 11.00 | 33.42 | 1.601 \pm .007 | 183.51 \pm 1.36 | .36 | 55.27 | 2.649 \pm .065 | .965 | .033 |
| CdSnP ₂ :Cu #5 | 161.60 \pm .04 | 12.06 | 33.35 | 1.597 \pm .007 | 185.57 \pm 1.54 | .35 | 57.32 | 2.747 \pm .074 | 1.088 | .029 |
| Sn ₄ P ₃ (Avg) | | | | | 185.0 \pm 1.0 | | 56.8 | 2.72 \pm .05 | | |

secondary peak was 185.5 ± 1.5 and 183.5 ± 1.3 , respectively, with a relative intensity of about 3%. The relative intensity is equal to the ratio of the Sn atoms in the Sn_4P_3 configuration to the number in the CdSnP_2 configuration. Since there are four Sn atoms per Sn_4P_3 molecule, the mole percentage of Sn_4P_3 to CdSnP_2 is one-quarter their relative absorption peak intensities. The minimum for the Sn_4P_3 spectrum registered at channel #185 ± 1 . Thus, within experimental uncertainty, the secondary resonance isomer shift for the cooper-doped samples is equivalent to the Sn_4P_3 isomer shift calculated independently, and is equal to $V_2 = 2.73 \pm 0.05$ mm/sec. This would seem to indicate the presence of a small, yet detectable, quantity of Sn_4P_3 inclusions in the Cu-doped samples. Attempts were made to fit a second lorentzian line to the other spectra, but the process would not converge, thus contraindicating the presence of Sn_4P_3 .

Several conclusions about the role of Sn in CdSnP_2 can be drawn from the presence of a single, narrow resonance isomer shift of 1.601 mm/sec and a (χ^2) very nearly equal to 1.000. Firstly, the absence of any electric quadrupole splitting, which would appear as a broadening in the single peak, implies a tetrahedral coordination of Sn atoms as previously believed. Secondly, an isomer shift equal to

1.601 mm/sec implies the existence of sp^3 hybrid orbitals in the valence band. Sn in $CaSnO_3$ is four times ionized, i.e., no valence electrons, and produces a zero isomer shift. Sn(alpha), on the other hand, exists in a pure sp^3 configuration and has an isomer shift approximately equal to 2.0 mm/sec. Therefore, an isomer shift of 1.6 mm/sec indicates the addition of 5s and 5p electrons to the valence levels, with some shielding due to the presence of four phosphorus nearest neighbors. According to Figure 3.4, with $n_p = 3$, the number of 5s electrons is approximately equal to 0.9, indicating a tendency towards dehybridization and partial ionic bonding with its P nearest neighbors.

4. PHOTOELECTROCHEMICAL CHARACTERIZATION

The binary III-V compound InP exhibits promise as a semiconductor electrode in photoelectrochemical (PEC) and photoassisted electrolysis (PAE) cells. The purpose of this part of our study is to investigate the potential of the isoelectronic analog of InP, CdSnP₂, in the role of semiconductor electrode in PEC cells.

CdSnP₂ crystals from all runs were mounted as electrodes and subsequently introduced as the working electrode in a PEC cell. Three different redox electrolyte solutions were investigated and analyzed on the basis of cell performance. Only polysulfide solution yielded reasonable results, while vanadium and ferrocyanide solutions did not.

Quantitative investigation of CdSnP₂ included photocurrent-voltage, photocurrent-spectra, and Mott-Schottky measurements. Subsequent analysis of PEC cell performance in the above modes yielded characteristic properties including doping density, energy gap, and flat-band potential, to mention a few.

The photocurrent-voltage measurement was also employed as a screening mechanism to selectively eliminate electrodes with sub-standard performance. Additionally, qualitative considerations of electrode preparation

techniques and PEC characterization effectiveness were made.

4.1 PEC Theory

Photoelectrochemistry is based principally on the semiconductor electrode. It is the semiconductor's ability to absorb light and convert it to electrical and/or chemical energy that forms the basis for the semiconductor/liquid junction solar and photoelectrosynthetic cells. The advantages of such a cell over conventional p-n homo- and heterojunction photovoltaic cells are many. Perhaps the biggest advantage of a semiconductor liquid-junction, over solid-state junctions, is that a high percentage of the single crystal efficiency can be realized in a polycrystalline material, where the cost of production is considerably less.

A second advantage of the electrochemical photovoltaic cell is that it is the most easily constructed of all solar cells because all that needs to be done is to immerse a semiconductor electrode and another inert electrode into an appropriate redox electrolyte and connect them through an external load. However, its potential for use in multicell arrays is questionable.

The working mechanism of the PEC cell is as follows: electricity is produced when the electron-hole pairs produced by illumination of the semiconductor electrode are separated in the space charge layer near the semiconductor-

electrolyte interface, with the majority carrier being driven into the bulk of the material and finally through the external circuit, while the minority carrier is driven to the semiconductor-electrolyte interface. The minority carrier oxidizes or reduces (depending on whether the bulk material is n- or p-type) the redox species in the electrolyte while the majority carrier accomplishes the opposite reaction at the dark inert electrode.

One major problem exists in this configuration, that being photocorrosion caused by the oxidation or reduction of the semiconductor itself by the highly reactive minority carriers at the surface. This problem has been a primary obstacle in the development of PEC solar cells.

The electrochemical cell consists of the following: a metal contact, a semiconductor electrode, an electrolyte, a counter(dark) electrode (Pt), and another metal contact, as shown in Figure 4.1. The potential difference between the metal ends of the cell is called the electrode potential. Often, a reference electrode is introduced to define a reference potential.

The electrode potential is composed of the potential differences at the phase boundaries making up the circuit, such as that between the semiconductor and the electrolyte. It is within this region that we are most

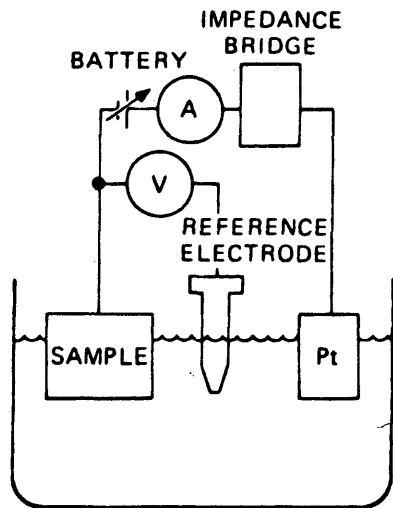


Figure 4.1. Schematic of cell featuring impedance (capacitive) measurement.

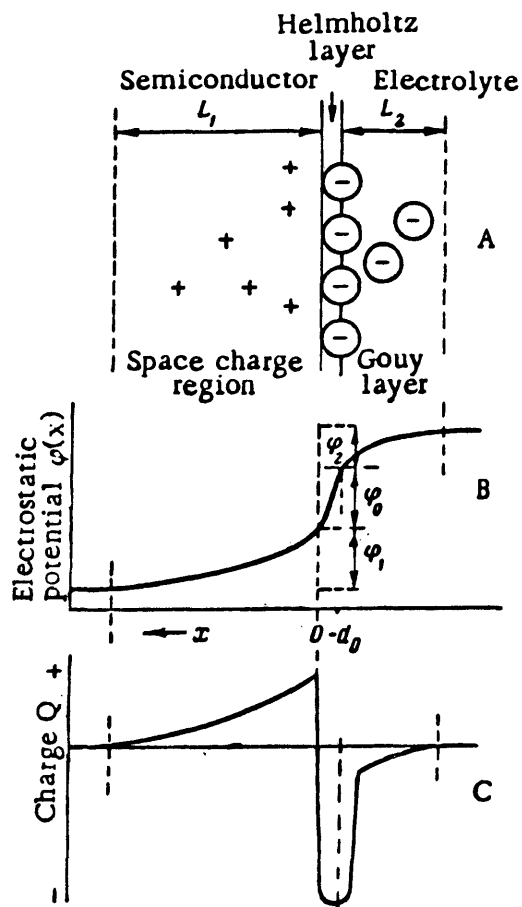


Figure 4.2
Structure of double layer (A) and distribution of potential (B) and charge (C) at the semiconductor - electrolyte interface.
(Myamlin & Pleskov, 1967)

interested in observing system changes.

The structure of the semiconductor-electrolyte interface, as well as the potential and charge distribution, is shown in Figure 4.2. The dense part of the double layer is formed of ions immediately adjacent to the semiconductor, and has a thickness determined by the radius of the ions, $\sim 10^{-8}$ cm. Electric fields and diffusion processes are the primary determinants of equilibrium ionic distributions and concentrations within the double layer and space charge region of the semiconductor. The interface structure discussed here, however, neglects oxide layers or layers of chemical species formed through reaction of the electrolyte with the semiconductor.

Characterization of the semiconducting material in the working electrode is accomplished by analyzing the response of the PEC cell under different conditions of illumination and applied bias. Three different modes of characterization are employed in this study and are summarized below.

| Measurement | Variable Parameter | Measured Parameter | Constant Parameter |
|----------------------|--------------------|--------------------|----------------------------|
| Photocurrent-Voltage | Cell Potential | Cell Current | Illumination (White light) |
| Photocurrent-Spectra | Wavelength | Cell Current | Cell Potential |
| Mott-Schottky | Cell Potential | Capacitance | Illumination (No light) |

Each mode will be discussed separately in terms of the physical models necessary to represent the system and the subsequent mathematical relations that result from the particular representation. From these mathematical relations one can extract the characteristic properties of the material, CdSnP₂.

We begin with an examination of the differential capacitance, which is the primary objective of Mott-Schottky measurements. The differential capacitance of an electrolyte-semiconductor contact is determined by the equation

$$C = \frac{dQ_2}{d\phi_{12}} = \frac{-dQ_1}{d\phi_{12}} \quad (4.1)$$

where ϕ_{12} is the total potential drop at the phase boundary and Q_2 and Q_1 are the ionic charges in the electrolyte and

space-charge region, respectively.

The contact capacitance of the 3-region system is essentially three capacitances in series: C_0 , C_1 , and C_2 , i.e., the capacitances of the Helmholtz layer, the space-charge region, and the diffuse part of the double layer in the electrolyte, respectively. Taking into account the form of the capacitances for each region, that is $C_n = \frac{\epsilon_n}{4\pi L_n}$ (20), and the order of magnitude of the Debye lengths ($L_1 \approx 10^{-4}$ cm, $L_0 \approx 10^{-8}$ cm, and $L_2 \approx 10^{-6}$ cm) (21) we find that the capacitance of the whole system is dominated by the capacitance of the space-charge region in the semiconductor, C_1 .

To obtain an expression for the relationship between C_1 and ϕ_{12} , we consider a relation derived from Poisson's equation (n-type bulk)

$$\frac{d^2V}{dx^2} = \left(\frac{N_d q}{\kappa \epsilon_0} \right) [\exp(-qV/kT) - 1] \quad (22) \quad (4.3)$$

where we assume N_d positive charges in the depletion region, and we are assuming $n = N_d \exp(-eV/kT)$ electrons in the conduction band. On integrating, with $\frac{dV}{dx} = 0$ when $V = 0$, we have

$$\left(\frac{dV}{dx} \right)^2 = \left(\frac{2qN_d}{\kappa \epsilon_0} \right) \left(V + \frac{kT}{q} [\exp(-qV/kT) - 1] \right) \quad (4.4)$$

At the surface, $V = V_s = \phi_{12} - V_{fb}$, and the exponential factor is negligible. From Gauss' law ($A \equiv$ electrode area)

$$\left(\frac{dV}{dx}\right)_{V=V_s} = \frac{Q_1}{\kappa\epsilon_0 A} \quad (4.5)$$

Upon substituting equation 4.5 into 4.4, and differentiating Q_1 with respect to ϕ_{12} , we obtain

$$\frac{1}{C^2} = \left(\frac{2}{qN_d\kappa\epsilon_0 A^2}\right)\left(\phi_{12} - V_{fb} - \frac{kT}{q}\right) \quad (4.6)$$

Two important parameters can be extracted from this relation; the flat-band potential, V_{fb} (intercept) and the doping density, N_d (slope). Values of the differential capacitance are acquired through measurements of the ac impedance between the sample and inert electrode.

Both photocurrent-voltage and photocurrent-spectra measurements rely on the Gartner model (23) for depletion-layer photoeffects in semiconductors. The total photocurrent density under monochromatic illumination and reverse bias (band-bending) conditions is given by

$$J_{tot} = -q\phi\left[1 - \frac{e^{-\alpha w}}{1 + \alpha L_p}\right] - \frac{qp_0 D_p}{L_p} \quad (4.7)$$

with α : absorption coefficient (cm^{-1})
 W : space charge layer width (cm)
 L_p : minority carrier diffusion length (cm)
 ϕ : total incident photon space flux ($\#/\text{cm}^2\text{-sec}$)
 D_p : diffusion coefficient for holes (cm^2/sec)
 p_0 : equilibrium hole density ($\#/\text{cm}^3$)

To determine the optical bandgap from the above relation, we proceed as follows. For αL_p and αW much less than one, we can expand J_{tot} and obtain

$$J_{\text{tot}} = -q\phi\alpha[L_p + W] \quad (4.8)$$

Near the absorption edge, α can be described as (24)

$$\alpha = \frac{A(h\nu - E_g)^{n/2}}{h\nu} \quad (4.9)$$

($n = 1$ for direct transition)

Therefore, the dependence of the photocurrent on the energy $h\nu$ of the incident exciting photon, for a direct transition, is

$$J_{\text{tot}} = \frac{C(h\nu - E_g)^{1/2}}{h\nu} \quad (4.10)$$

Thus, a plot of $J^2(h\nu)^2$ vs $h\nu$ can yield E_g values for direct allowed transitions.

To determine values for the flat-band potential and diffusion length of minority carriers, we can solve the above relation (equation 4.7) for J_{tot} in terms of applied cell bias. If $\alpha L_p \ll 1$, then

$$\begin{aligned} J_{tot} &= q\phi(1 - e^{-\alpha w}) & (4.11) \\ &\approx q\phi\alpha w, \quad \alpha w < 1 \end{aligned}$$

The depletion layer region width, w , is given by the relation (25)

$$w = \left(\frac{2\epsilon}{qN_d}\right)^{1/2} (V - V_{fb})^{1/2} \quad (4.12)$$

thus

$$J = q\phi\alpha \left(\frac{2\epsilon}{qN_d}\right)^{1/2} (V - V_{fb})^{1/2} \quad (4.13)$$

and a plot of J^2 vs V will yield an intercept equal to V_{fb} .

To determine the absorption coefficient, α , and the diffusion length of minority carriers, L_p from photocurrent measurements, we write equation 4.7 in the form

$$\ln(1 - \phi) = -\alpha \left(\frac{2\epsilon}{qN_d}\right)^{1/2} (V - V_{fb})^{1/2} - \ln(1 + \alpha L_p) \quad (4.14)$$

where ϕ is the quantum efficiency of the material, and N_d is known. Thus, plotting $\ln(1 - \phi)$ vs $(V - V_{fb})^{1/2}$, under reverse bias, we obtain α from the slope and L_p from the intercept.

4.2 Experimental Procedures

Semiconductor electrode preparation was accomplished and testing concluded in the PEC cell configuration.

8 mm (dia) × 20 cm glass tubes were heated and bent to assure proper crystal orientation relative to the illumination source. 2 × 10 mm copper plates were soldered to 22 ga. copper wire and threaded through the glass tubes. Single crystals of CdSnP₂ were mounted, as grown, to give the desired surface orientation. Ohmic contact was made by applying In-Ga eutectic to the front surface and then sealing with white epoxy such that only the desired crystal face was exposed. Originally, attempts to make ohmic contact were made by applying conductive silver epoxy to the back of single crystals. However, crystals with layered and stacked morphologies, as well as those with open inclusions, were highly resistive front to back. When necessary, the exposed crystal surface was cleaned with the crystal etchant discussed earlier.

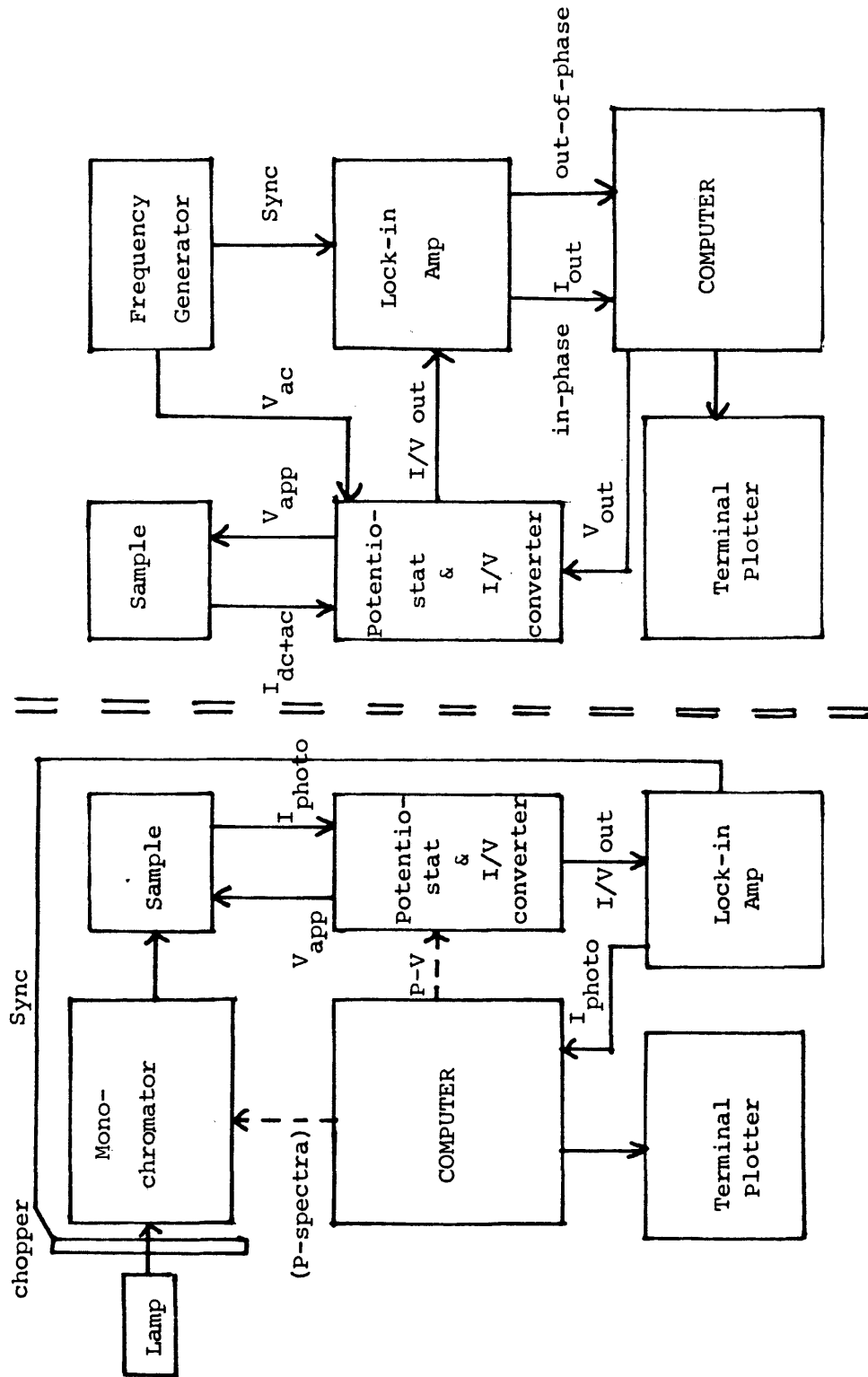
Photocurrent and capacity measurements were made in an electrochemical cell with a Pt counter-electrode and an SCE (saturated calomel electrode) as a reference. P-type crystals were employed as photocathodes, while n-type crystals were photoanodes in the PEC cell. A 3:3:4 polysulfide solution was utilized as the redox electrolyte

[3M(S²⁻):3M(S₂²⁻):4M(potassium hydroxide)]. Polysulfide is a versatile redox for both oxidation ($2S^{2-} - 2e \rightarrow S_2^{2-}$), at n-type surfaces, and reduction ($S_2^{2-} + 2e \rightarrow 2S^{2-}$), at p-type surfaces, are allowed and thus both n- and p-type materials can be tested. The solution potential is a stable $-0.72V$ (SCE) and can often be used without a reference electrode.

Data acquisition and subsequent analysis was performed by either the MODCOMP/CAMAC Data Acquisition or the DECLAB/11 MNC computing systems. A block diagram showing the experimental apparatus and related electronics is shown in Figure 4.3. For the photocurrent-voltage and -spectra measurements, the applied potential and incident photon wavelength (chopped) were controlled by the computer. Resultant sample photocurrent was fed into an I/V converter, whose output voltage (chopped) was then fed into a synchronized lock-in amplifier where the actual photocurrent signal is separated from the background signals and noise. The resultant signal is fed into the computer for data acquisition and analysis.

Mott-Schottky capacity measurements were performed in a similar manner. A small ac signal is superimposed on a dc potential and applied to the PEC cell. Resultant currents (ac and dc) pass through a I/V converter and then

Figure 4.3 Block diagram of experimental set-up and related electronics.



Mott-Schottky capacity set-up

Photocurrent-voltage & Spectra set-up

on to a lock-in amplifier where the in-phase and out-of-phase components are separated and passed on to the computer for analysis.

The extraction of various material parameters was accomplished either directly by computer calculation or by analysis of computer generated plots.

4.3 Results and Discussion

One representative electrode for each set of Cu-doped and undoped samples was quantitatively analyzed as a semiconductor electrode in a PEC cell. Both crystal samples were from run #6 due to prior problems in mounting.

Quantitative results were obtained and conclusions drawn for the n-CdSnP₂ sample electrode, while only qualitative conclusions could be drawn from results obtained with CdSnP₂:Cu. The results for n-type crystals are discussed first and summarized in Table 4.1, alongside previously published results.

Table 4.1.

Properties of n-CdSnP₂ from PEC Characterization

| Property | PEC Value | Other Known Value | Ref |
|----------------|---|--|----------|
| N _d | 8.0 × 10 ¹⁷ /cm ³ | (3-5) × 10 ¹⁷ /cm ³ | (26) |
| μ(Hall) | 290 cm ² /V-s | 1100-2000 $\frac{\text{cm}^2}{\text{V-s}}$ | (27, 29) |
| E _g | 1.17, 1.23, & 1.37 eV | 1.16, 1.24, 1.32 | (28) |
| ρ(Hall) | 4.7 × 10 ⁻² ohm-cm | 10 ⁻¹ → 10 ³ ohm-cm | (26, 29) |
| L _p | .10 μm | -- | |
| α | 5.6 × 10 ⁴ cm ⁻¹ (λ = 1050 nm) | 1-10 × 10 ⁴ cm ⁻¹ (λ = 1050 nm) | (29) |

Mott-Schottky results (Figure 4.4) indicate a flat-band potential of $V_{fb} = -1.17$ V (SCE) and a doping density of $N_D = 8.0 \times 10^{17}/\text{cm}^3$. The doping density agrees with values quoted in refs. (26) and (27) and with Hall measurements conducted independently. The extent of the linear region implies a small experimental uncertainty, on the order of $\pm 5\%$, in N_D and V_{fb} .

From photocurrent-spectra analysis (Figure 4.5(a)), three direct allowed transitions can be extracted. They are $E_g = 1.17, 1.23$ and 1.37 eV. They correspond, respectively, to $\Gamma_7-\Gamma_6$ ($||, \perp$), $\Gamma_6-\Gamma_6$ (\perp), and $\Gamma_7-\Gamma_6$ ($\perp, ||$) transitions, as seen in Figure 4.5 (b). The values quoted above agree well with values obtained through electroreflectance data (28). The uncertainties in the lowest two values of E_g determined from our photocurrent analysis are likely to be small considering the wide linear region used in the analysis. However, for $E_g = 1.37$ eV, the linear region does not have definitive boundaries. The error is on the order of ± 0.05 eV.

An examination of the J vs $h\nu$ plot of Figure 4.6 indicates the onset of significant photocurrent near the band edge at 1.15 eV. For a pure direct transition, the onset of photocurrent should be sharper, but the shape still substantiates the direct transition proposition.

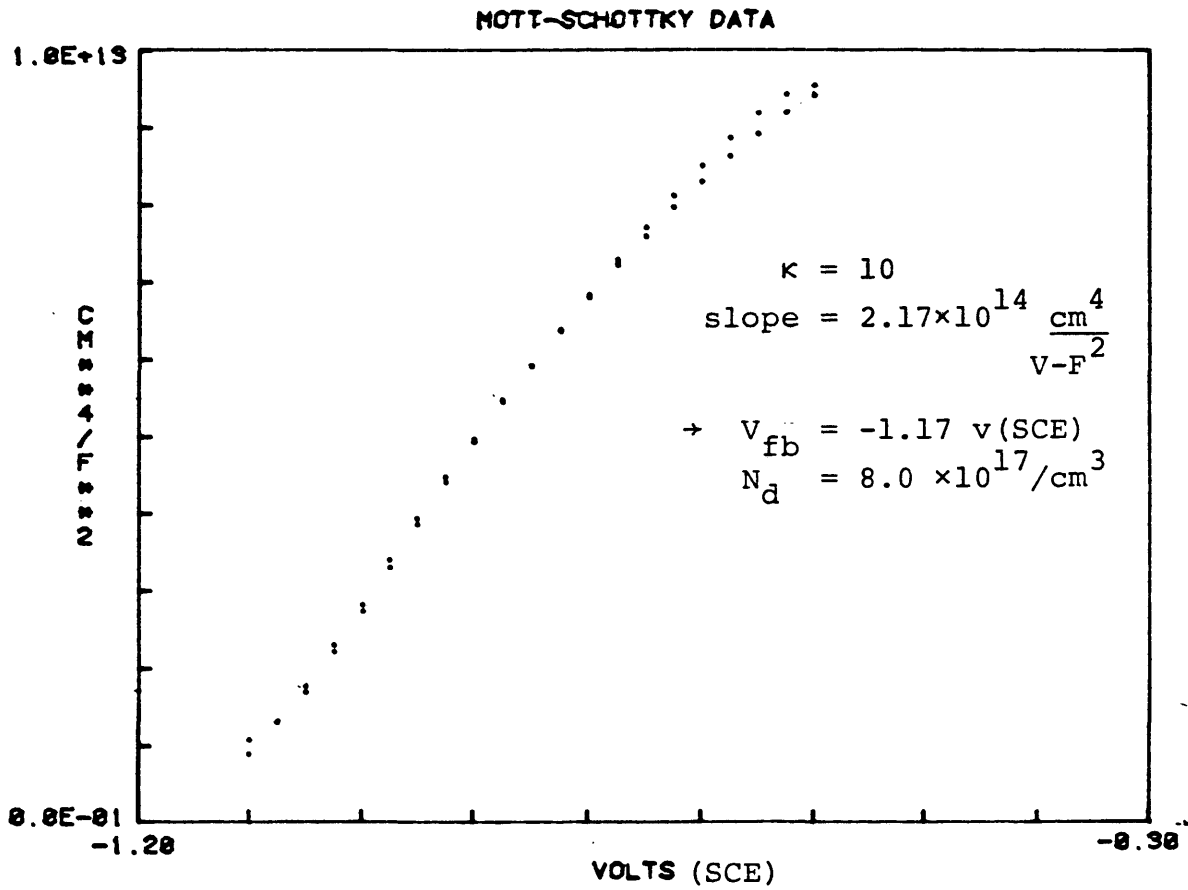


Figure 4.4 Mott-Schottky analysis of n-CdSnP₂.
 ($1/C^2$ vs V_{cell})

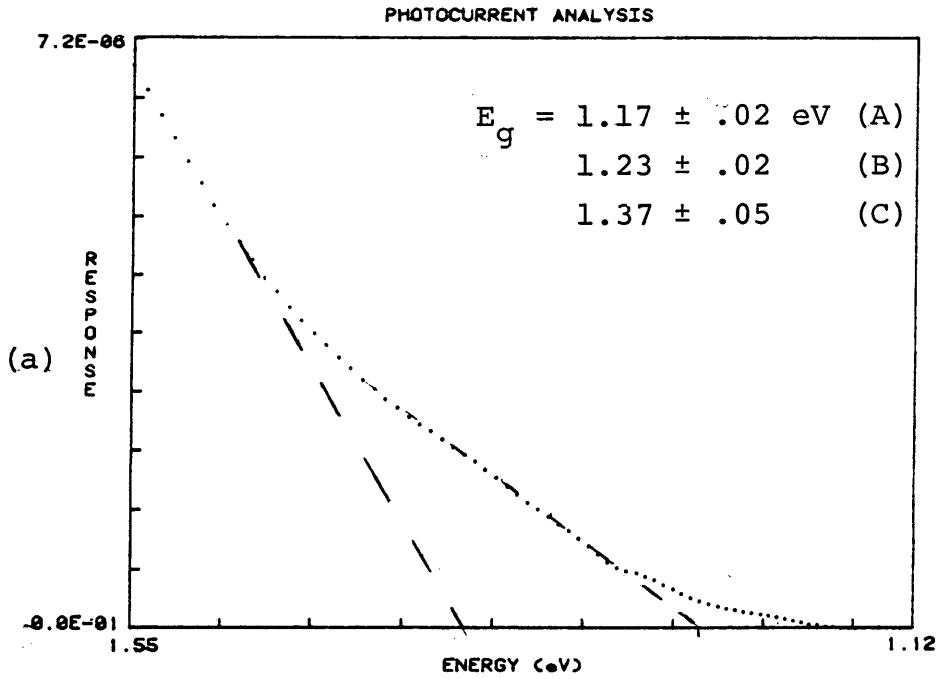
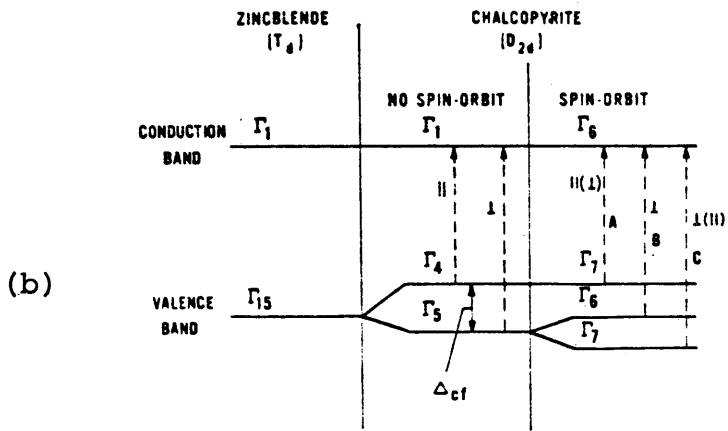


Figure 4.5 Photocurrent-spectroscopy analysis of $n\text{-CdSnP}_2$ ($J^2(h\nu)^2$ vs. $h\nu$) and description of transitions.



Band structure and selection rules for the transitions in a chalcopyrite crystal derived from the $\Gamma_{15} \rightarrow \Gamma_1$ energy gap in a zincblende crystal. (Shay *et al.*, 1970 a.)

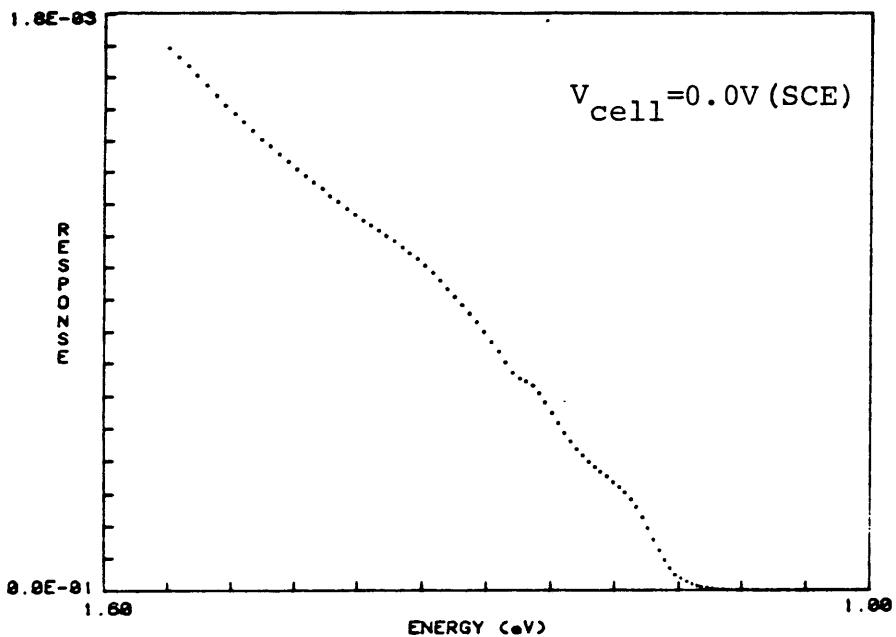


Figure 4.6 Photocurrent-spectroscopy analysis (J vs hv)

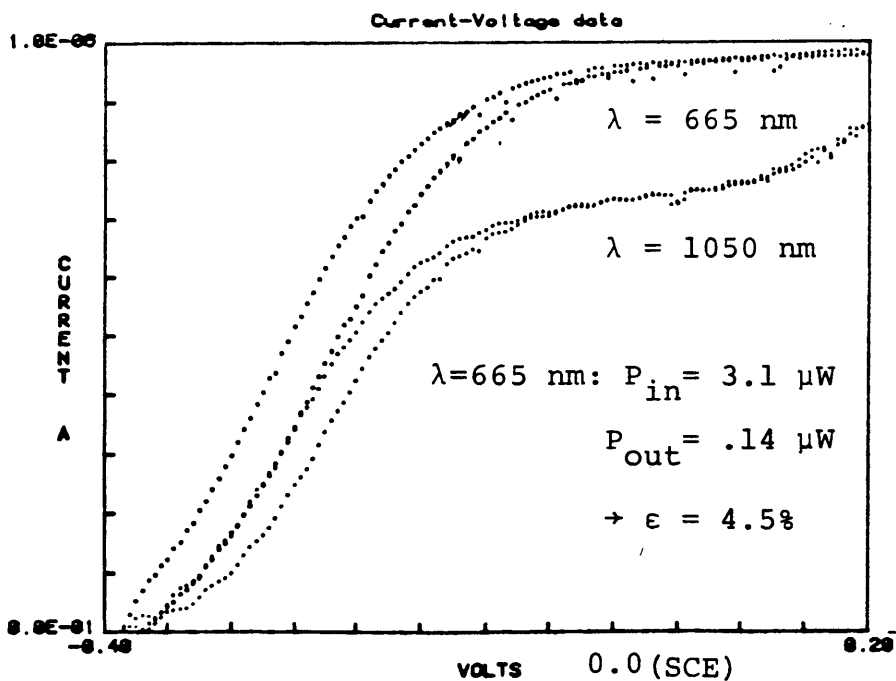


Figure 4.7 Photocurrent-voltage analysis (J vs V)

A photocurrent-voltage plot is shown in Figure 4.7 for two incident photon wavelengths: $\lambda = 665$ nm and 1050 nm. The onset of photocurrent, as a function of voltage, is not ideal. However, a cell efficiency of 4.5% was calculated from an incident flux of $3.1 \mu\text{W}$ at $\lambda = 665$ nm. This can be considered good considering the crudeness of the sample and electrode preparation, and the likelihood that polysulfide is not the best redox for CdSnP_2 . A flat-band potential of approximately $-.4$ V (poly. ref.) can be seen and agrees, to within 10%, with the value determined from M-S measurements [-1.17 V (SCE) + $.72$ V (poly pot) = $-.45$ V (poly ref)].

From a plot of $\ln[1 - \phi]$ vs $\text{sqrt}[V - V_{fb}]$ ($\lambda = 1050$ nm,), considering the linear region between .55 and .70 and a doping density of $N_d = 8.0 \times 10^{17}/\text{cm}^3$, an absorption coefficient, $\alpha = 5.60 \times 10^4/\text{cm}$, and a diffusion length of minority carriers, $L_p = .11 \mu\text{m}$, are calculated from the slope and intercept, respectively (Figure 4.8). The value for α falls within the range expected for $\lambda = 1050$ nm (20). The value for L_p quoted is one of the first obtained for CdSnP_2 .

Independent values for doping density, resistivity, and mobility for crystals from run #6 were obtained from Hall effect measurements. Values of $N_d = 4.58 \times 10^{17}/\text{cm}^3$, $\mu = 290 \text{ cm}^2/\text{V-s}$, and $\rho = 4.7 \times 10^{-2} \text{ ohm-cm}$ were found. N_d

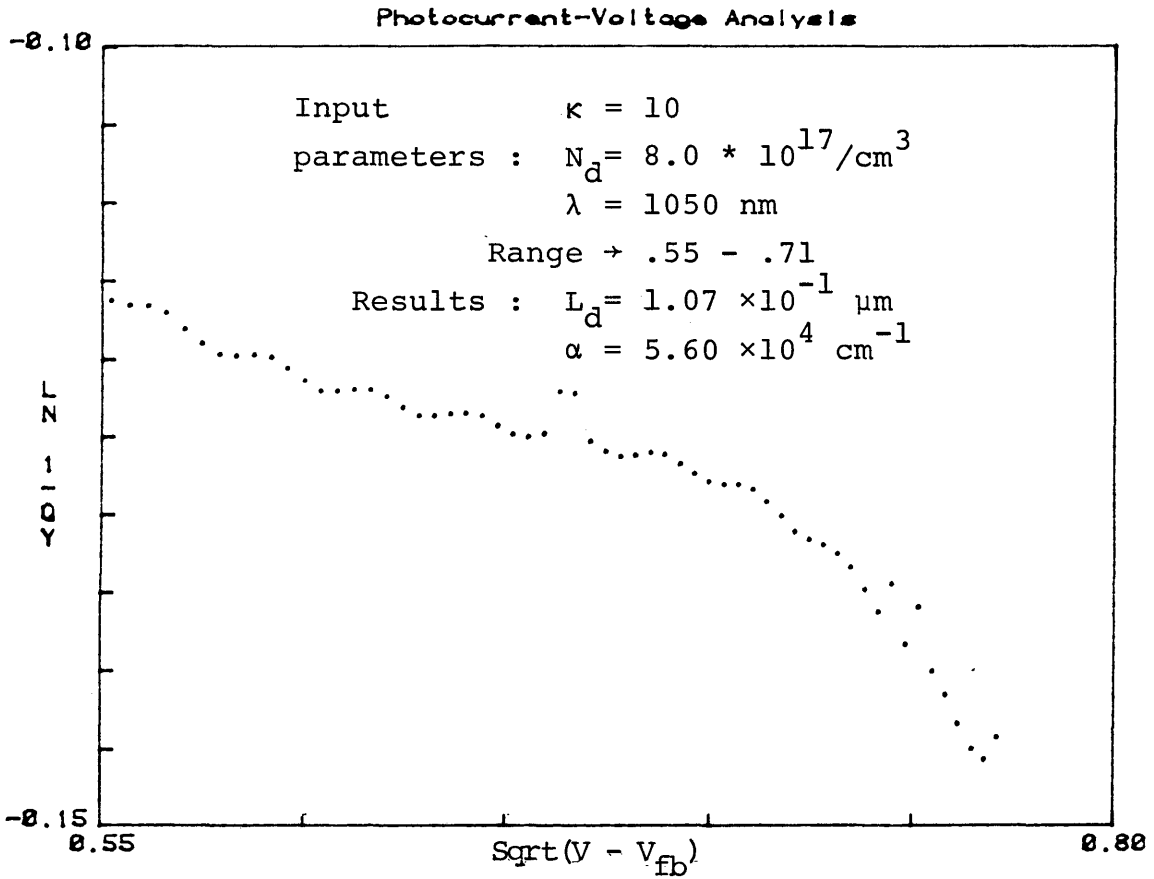


Figure 4.8 Photocurrent - voltage analysis
 ($\ln(1-\phi)$ vs Sqrt(V-V_{fb}))

(Hall) agrees with N_D (PEC), but the μ (Hall) are quite low compared to values of $2000 \text{ cm}^2/\text{V-s}$ determined by Shay, et al. This is possibly due to a high lattice defect density resulting from our temperature spiking.

Our results from $\text{CdSnP}_2:\text{Cu}$ were both contradictory and inconclusive. Analytical calculations of characteristic properties was essentially impossible due to the frequency of apparently contradictory data and typically low responses that were affected by system noise.

Mott-Schottky measurements (Figure 4.9) indicate both n- and p-type behavior. Extrapolation of a linear region in the n-type region gives a $V_{fb} = -1.19 \text{ V}$ (SCE) and a donor density $N_D = 2.7 \times 10^{14}/\text{cm}^3$, thus implying for that potential region a compensated n-type crystal. Analysis of the p-type region produced contradictory results.

Photocurrent-spectra measurements (Figure 4.10) seem to indicate both n- and p-type behavior, as well as suggesting sub-bandgap photoconductivity possibly due to potential induced copper states within the forbidden region. At 0.0 V (SCE), the behavior is basically n-type with photo-response beginning at the band edge. Zero volts SCE is a reverse-bias condition for a p-type material and therefore should show little current response. However, this is obviously not the case, and it appears there is a

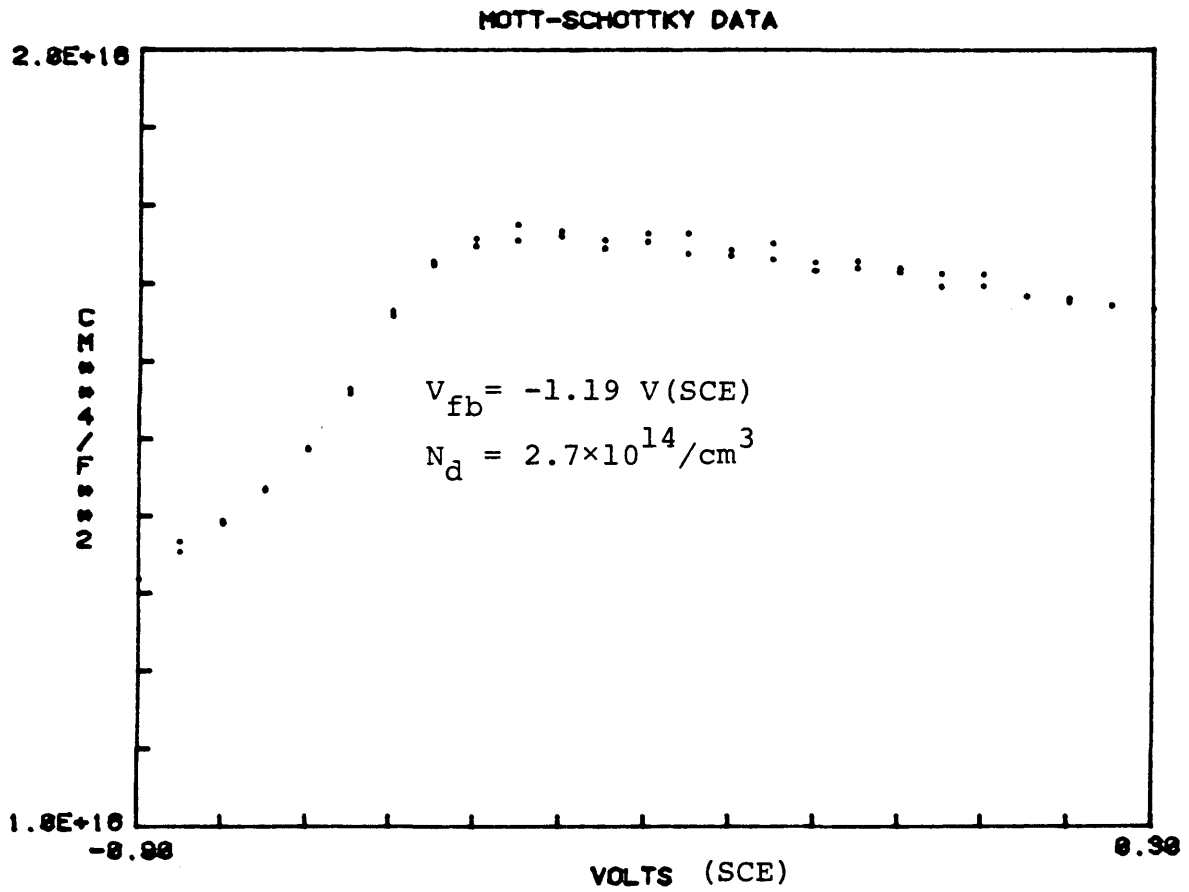


Figure 4.9 Mott- Schottky analysis of p-CdSnP₂:Cu

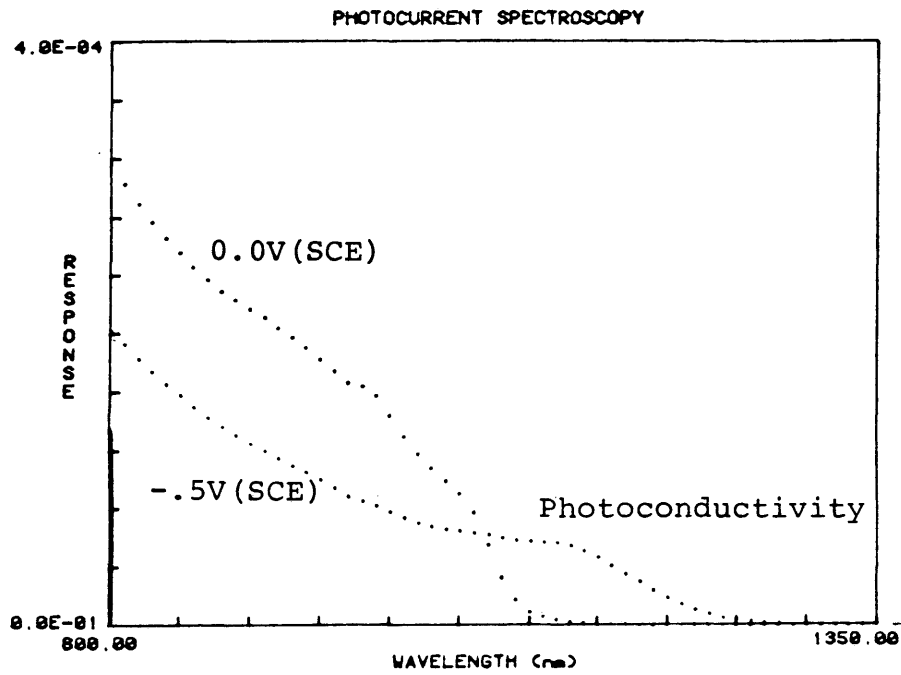
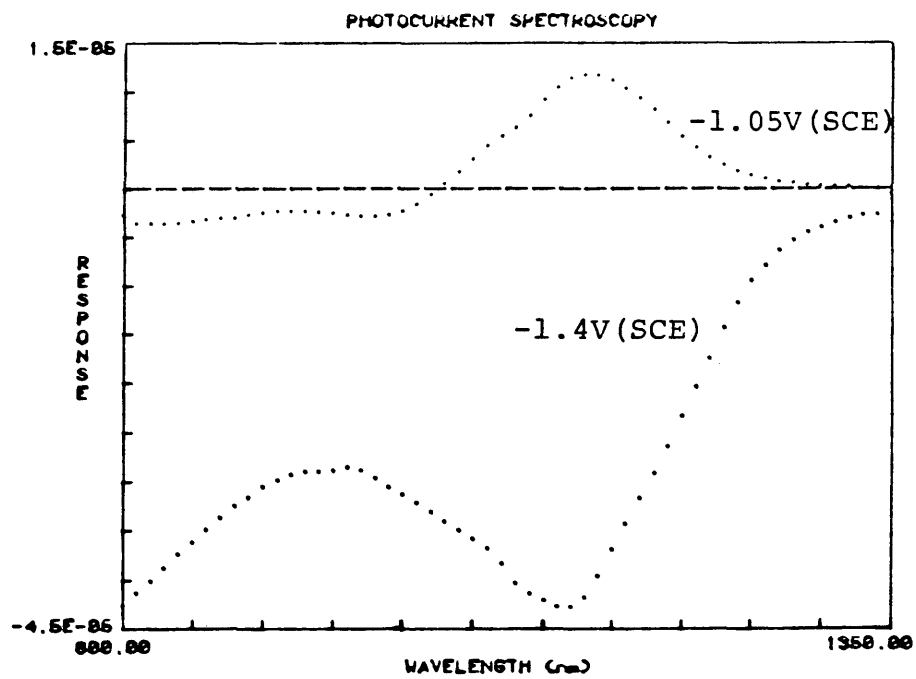


Figure 4.10 Photocurrent spectroscopy of CdSnP₂:Cu at four potentials.



potential dependence of the occupancy of Cu-related acceptor levels.

As the potential is made more negative, the forward current decreases, but begins to appear at lower energies. This implies transitions from or to sub-bandgap states, and photoconductivity begins. Photoconductivity can be defined here as the excitement of carriers to states below the conduction band.

When the cell bias is further reduced to the flat-band potential of ~ -1.1 V (SCE), the current reverses direction for photo energies greater than E_g , but continues to flow in the forward direction for sub-bandgap energies due to the photoconductivity effect. Acceptor levels begin to dominate due to the appearance of new multi-charge centers (30). As the potential is further increased in the negative direction, negative photoconductivity dominates and a "pseudo" p-type material emerges with a bandgap less than 1.0 eV. Acceptor levels within the forbidden zone dominate. There is a relative peak at $E_v = 1.30$ eV, indicating a compensation effect by the flow of conduction electrons at the high direct bandgap. The mobility of these multicharge centers would appear to be low because the sample resistivity increases significantly at the negative cell biases, as can be seen in Figure 4.11.

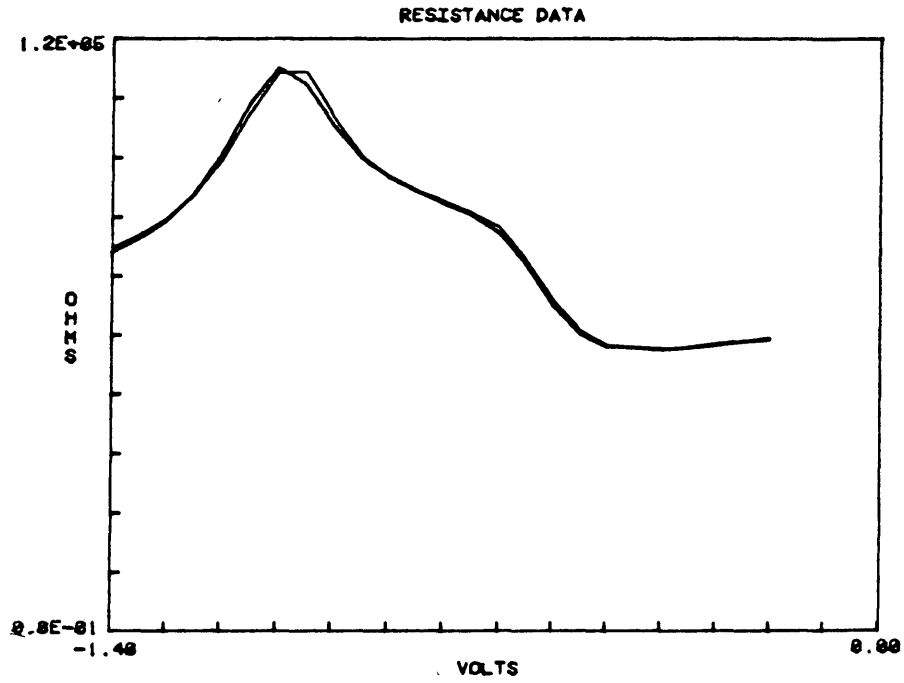


Figure 4.11 Resistivity measurements of $p\text{-CdSnP}_2\text{:Cu}$.

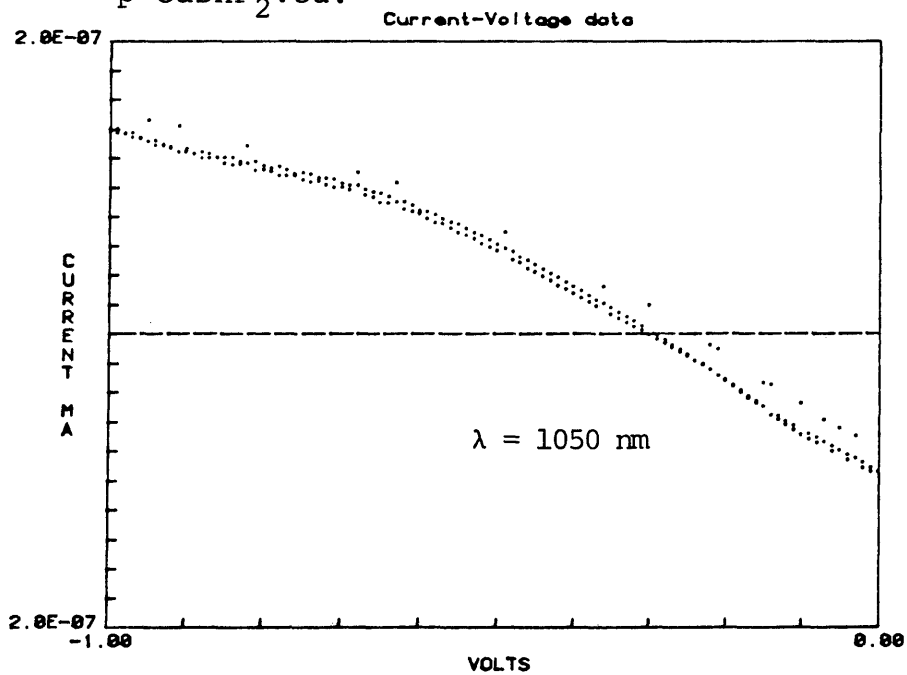


Figure 4.12 Photocurrent-voltage plot of $p\text{-CdSnP}_2\text{:Cu}$.

Photocurrent-voltage data (Figure 4.12) further substantiates the transition from n- to p-type conductivity at potentials of $-0.3 \text{ V (poly)} \cong -1.0 \text{ V (SCE)}$. From a plot of J^2 vs V (Figure 4.13), a flat-band potential of approximately $-0.2 \text{ V (poly)} \cong -0.9 \text{ V (SCE)}$ is seen.

Analysis of the $\ln(1 - \phi)$ vs $\sqrt{V - V_{fb}}$ plot (Figure 4.14) determines values for α and L_n of 1861 cm^{-1} and $.10 \text{ }\mu\text{m}$, respectively, assuming $N_A \cong 1 \times 10^{16}/\text{cm}^3$. The value for α is extremely low and suggests the analysis does not apply in this case. Values for the hole-density in p-type materials were acquired from Hall effect measurements. Values for resistivity and hole mobility, ρ and μ_h , of 51.6 ohm-cm and $9. \text{ sec}^2/\text{V-s}$, respectively, were also determined from Hall measurements. These values, as well as the other characteristic properties calculated, suggest poor semiconducting ability and are the main reason for considering other dopants in attempts to produce p-CdSnP₂.

In conclusion, it would appear that PEC characterization of n-CdSnP₂ indicates potential for use in photovoltaic and photoelectrochemical devices. The direct energy band gaps observed are within the optimum range, $1.0\text{-}1.5 \text{ eV}$, and adequate electron densities can be achieved without impurity doping. However, the crystals grown for

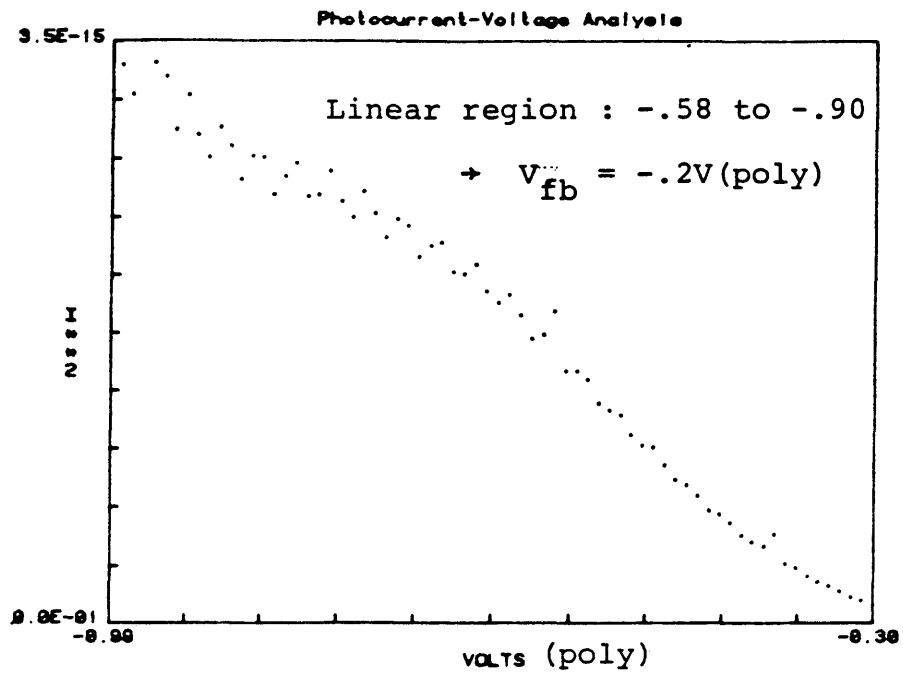
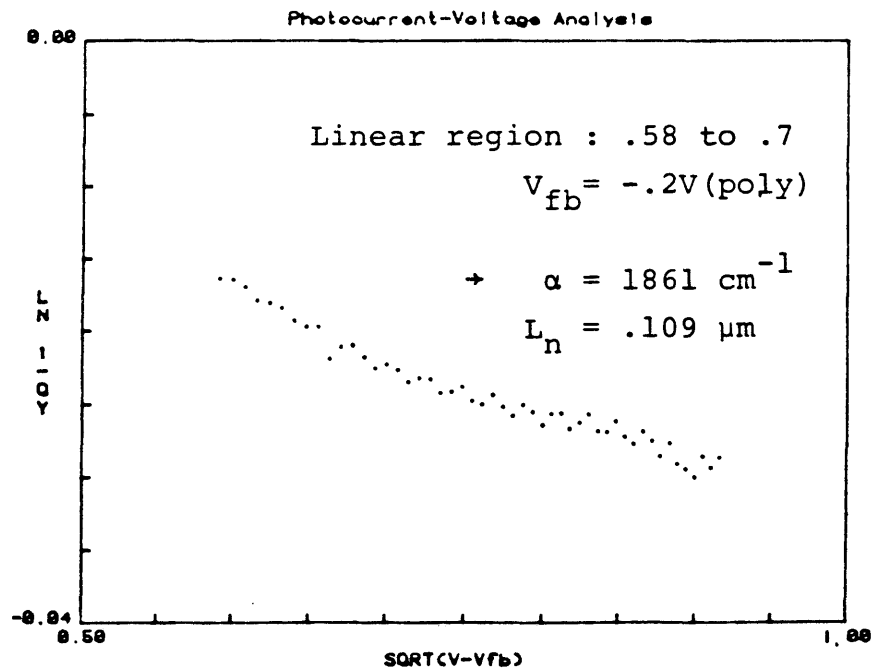


Figure 4.13 Photocurrent-voltage analysis.

Figure 4.14 Photocurrent-voltage analysis of p-CdSnP₂:Cu.

this study exhibit low mobilities, suggesting the necessity for further studies.

$\text{CdSnP}_2:\text{Cu}$, on the other hand, does not exhibit much potential for PEC applications. Though the material might have PV applications, when introduced as a semiconductor electrode, the copper dopant seems to adversely affect its performance. However, some interesting physical phenomena are observed and lend insight into the electronic structure of intrinsic CdSnP_2 .

Conclusion

This study hereto conducted on the semiconducting material CdSnP_2 can only be considered preliminary. Although several definitive conclusions can be drawn about the material and its characteristic properties, the study has opened even more channels of possible research efforts.

The growth of single crystals of CdSnP_2 was accomplished by the solution growth technique. Single crystal size was enhanced through temperature profiling, but there is likely a limit. Furthermore, there are clear indications that enhancing crystal size by the methods employed in this study actually may affect material properties in a negative way. Possibly, solution growth in a different solvent, such as Cd, may yield better crystals, but there is no evidence to substantiate this. Further studies on crystal growth methods is necessary.

The XRD studies conducted did not lend any additional information of the structure of CdSnP_2 beyond what is already known, but it did substantiate that our solution growth techniques were successful. MES studies, on the other hand, shed some light on the effects of doping crystals with elemental copper. Though the connection is not yet seen, $\text{CdSnP}_2:\text{Cu}(.5\%)$ samples seem to have or include a finite percentage of Sn_4P_3 inclusions or

impurities. This was seen as a second independent resonance in the Mössbauer spectra with an isomer shift at 2.72 mm/sec. The single narrow isomer shift at 1.601 mm/sec substantiated the proposition that Sn exists in a tetrahedrally coordinated sub-lattice and that the electronic configuration of the valence levels approaches that of a sp^3 hybrid orbital.

The PEC measurements conducted and reported here on $CdSnP_2$ are probably the first of their kind. It should also be mentioned that this method of material characterization is still in the development stages. Both doped and undoped $CdSnP_2$ samples were introduced as the working electrode in a PEC cell, with polysulfide solution as the redox electrolyte, and subsequently tested under various biasing and illumination conditions. Testing of n- $CdSnP_2$ proved successful, whereas p- $CdSnP_2:Cu$ testing was not. It is possible that the Sn_4P_3 inclusions reported earlier are a cause of poor p- $CdSnP_2:Cu$ behavior.

Capacity measurements yielded doping densities of $10^{17}/cm^3$ and more, and flat-band potentials relative to SCE of -1.17 V. Photocurrent-voltage measurements indicate cell efficiencies of 4.5%, absorption coefficients of $10^5 cm^{-1}$, and diffusion lengths of minority carriers of $10^{-1} \mu m$. Photocurrent-spectra analysis indicated direct allowed

transitions at 1.17, 1.23 and 1.37 eV for n-CdSnP₂, and substantial photoconductivity in p-CdSnP₂:Cu. Many more conditions of cell bias and incident illumination could be tested. Methods of electrode preparation, involving In-Ga contacts, could be improved upon.

Further investigation of this ternary semiconducting material, CdSnP₂, is definitely warranted.

References

1. S. W. Angrist, Direct Energy Conversion, Allyn & Bacon, 177 (1982).
2. S. W. Angrist, Direct Energy Conversion, Allyn & Bacon, 177 (1982).
3. N. A. Reddy, High Temp. Thermal Expansion Study of Cadmium-Stanni Disphosphide by an X-ray Method, J. Phys. D., 15, 2247-2253 (1982).
4. J. F. Alward, Band Structures and Optical Properties of CdSnP_2 and CdSnAs_2 , Phys. Rev. B, 57, 625-629 (1979).
5. J. L. Shay, and J. H. Wernick, Ternary Chalcopyrite Semiconductors: Growth, Electronic Properties, and Applications, Pergamon Press (1975).
6. J. L. Shay and J. H. Wernick, Ternary Chalcopyrite Semiconductors: Growth, Electronic Properties, and Applications, Pergamon Press (1975).
7. E. P. Trifonova, n-n Heterojunction CdSnP_2 -InP, Phys. Stat. Sol. (a), 38, K37-39 (1976).
8. J. L. Shay and J. H. Wernick, Ternary Chalcopyrite Semiconductors: Growth, Electronic Properties, and Applications, Pergamon Press, p. 100, 1975.

9. I. P. Akimchenko, Impurity Photoconductivity of CdSnP₂ Single Crystals, Phys. Stat. Sol. (a), 3, K51-53 (1970).
10. T. Matsumoto, Etching Study on CdSnP₂ Prismlike Crystals, J. crystal. Growth, 51, 143-146 (1980).
11. V. I. Danilov, Effect of Polarity on Properties of CdSnP₂ and CdSnAs₂ Crystals Grown from Melt, J. Sov. Phys., 11, 49-52 (1980).
12. T. Matsumoto, Etching Study on CdSnP₂ Prismlike Crystals, J. Crystal. Growth, 51, 143-146 (1980).
13. J. L. Shay and J. H. Wernick, Ternary Chalcopyrite Semiconductors: Growth, Electronic Properties and Applications, Pergamon Press, p. 3, 1980.
14. J. L. Shay and J. H. Wernick, Ternary Chalcopyrite Semiconductors: Growth, Electronic Properties and Applications, Pergamon Press, p. 3, 1980.
15. J. L. Shay and J. H. Wernick, Ternary Chalcopyrite Semiconductors: Growth, Electronic Properties and Applications, Pergamon Press, p. 3, 1980.
16. Joint Committee on Powder Diffraction Studies, 1972.
17. G. K. Shenoy and F. E. Wagner, Mössbauer Isomer Shifts, North-Holland, 41 (1978).

18. S. L. Ruby and G. B. Beard, Interpretation of Mössbauer Measurements in Tin and Antimony, *Physical Review*, 159, 239-245 (1967).
19. G. K. Shenoy and F. E. Wagner,¹ Mössbauer Isomer Shifts, North-Holland, 41 (1978).
20. Victor A. Myamlin and Yurii V. Pleskov, *Electrochemistry of Semiconductors*, Plenum Press, p. 57, (1967).
21. Victor A. Myamlin and Yurii V. Pleskov, *Electrochemistry of Semiconductors*, Plenum Press, p. 36, (1967).
22. S. Roy Morrison, *Electrochemistry at Semiconductor and Oxidized Metal Electrodes*, Plenum Press, p. 127, (1980).
23. W. W. Gartner, *Physical Review*, 116, 84 (1959).
24. J. I. Pankove, *Optical Processes in Semiconductors*, Kover Publications, (1971).
25. Yehudith Mirovsky and David Cahen, Photoelectrochemical Solar Cells: Interpretation of Cell Performance using Electrochemical Determination of Photoelectrode Properties, *Thin Solid Films*, 91, 349-355 (1982).
26. E. Ziegler, Electrical Properties of n-CdSnP₂, *Phys. Stat. Sol (a)*, 57, 625-629 (1980).

27. I. A. Karpovich, Hall Mobility of Electrons in CdSnP₂ Single Crystals, Sov. Phys. Semi., 10, 594-95 (1976).
28. G. F. Karavaev, Electroreflectance Spectra and Energy Band Structure of CdSnP₂, Phys. Stat. Sol. (a), 45, 443-451 (1971).
29. J. L. Shay, J. H. Wernick, Ternary Chalcopyrite Semiconductors: Growth, Electronic Properties, and Applications, Pergamon Press, p. 99, (1980).
30. I. P. Akimchenko, Impurity Photoconductivity of CdSnP₂ Single Crystals, Phys. Stat. Sol. (a), 3, K51-53 (1970).

Appendix 1

Derivation of Structure Factor and Calculation of Allowed Miller Indices (hkl) for CdSnP₂.

$$S(\vec{K}) = \sum_{\alpha=1}^3 f_{\alpha} \sum_{j=1}^{n_{\alpha}} \exp[i(\vec{k} \cdot \vec{d}_j)_{\alpha}] ; \quad \begin{array}{l} \alpha = 1, 2, 3 \rightarrow \text{Cd, Sn, P} \\ n_{\alpha} = 4, 4, 8 \end{array}$$

$$\vec{K}_{\alpha} = 2\pi \left(\frac{h}{a} \hat{x} + \frac{k}{a} \hat{y} + \frac{l}{c} \hat{z} \right); \quad f_{\alpha} = 1.0, 1.0, 0.3^*$$

Equivalent positions

$$\begin{aligned} \text{Cd: } \vec{d}_1 &= \hat{o}; \quad \vec{d}_2 = \frac{a}{2} \hat{y} + \frac{c}{4} \hat{z}; \quad \vec{d}_3 = \frac{a}{2} \hat{x} + \frac{a}{2} \hat{y} + \frac{c}{2} \hat{z}; \\ \vec{d}_4 &= a\hat{x} + \frac{a}{2} \hat{y} + \frac{3}{4} c\hat{z} \end{aligned}$$

$$\begin{aligned} S_{\text{Cd}} &= \exp[i(\vec{K} \cdot \vec{d}_1)] + \exp[i(\vec{K} \cdot \vec{d}_2)] + \exp[i(\vec{K} \cdot \vec{d}_3)] + \\ &\quad \exp[i(\vec{K} \cdot \vec{d}_4)] \\ &= 1 + \exp[i\pi(K + \frac{l}{2})] + \exp[i\pi(h + k + l)] + \exp \\ &\quad [i\pi(h + \frac{3}{2} l)] \end{aligned}$$

$$\begin{aligned} \text{Sn: } \vec{d}_1 &= \frac{c}{2} \hat{z}; \quad \vec{d}_2 = \frac{a}{2} \hat{y} + \frac{c}{4} \hat{z}; \quad \vec{d}_3 = \frac{a}{2} \hat{x} + \frac{a}{2} \hat{y} + c\hat{z}; \\ \vec{d}_4 &= \frac{a}{2} \hat{x} + a\hat{y} + \frac{c}{4} \hat{z} \end{aligned}$$

$$\begin{aligned} S_{\text{Sn}} &= \exp[i\pi(l)] + \exp[i\pi(K + \frac{3}{2} l)] + \exp[i\pi(h + k + \\ &\quad 2l)] + \exp[i\pi(h + 2k + \frac{1}{2} l)] \end{aligned}$$

*Atomic form factor values here are for demonstration purposes. Relative values are approximately correct.

$$\begin{aligned}
P: \quad \vec{d}_1 &= -w\hat{x} + \frac{a}{4}\hat{y} + \frac{c}{8}\hat{z}; \quad \vec{d}_2 = w\hat{x} + \frac{3}{4}a\hat{y} + \frac{c}{8}\hat{z}; \\
\vec{d}_3 &= \frac{3}{4}a\hat{x} + w\hat{y} + \frac{7}{8}c\hat{z}; \quad \vec{d}_4 = \frac{a}{4}\hat{x} + w\hat{y} + \frac{7}{8}c\hat{z} \\
\vec{d}_5 &= (\frac{1}{2}a-w)\hat{x} + \frac{3a}{4}\hat{y} + \frac{5c}{8}\hat{z}; \\
\vec{d}_6 &= (w + \frac{1}{2}a)\hat{x} + \frac{a}{4}\hat{y} + \frac{5}{8}c\hat{z}; \\
\vec{d}_7 &= \frac{a}{4}\hat{x} + (\frac{1}{2}a-w)\hat{y} + \frac{3}{8}c\hat{z}; \\
\vec{d}_8 &= \frac{3a}{4}\hat{x} + (w + \frac{1}{2}a)\hat{y} + \frac{3}{8}c\hat{z} \\
w &= (.2621)a
\end{aligned}$$

$$\begin{aligned}
S_p &= \exp[i\pi (-\frac{2hw}{a} + \frac{k}{2} + \frac{1}{4})] + \\
&\quad \exp[i\pi (\frac{2hw}{a} + \frac{3}{2}k + \frac{1}{4})] + \\
&\quad \exp[i\pi (\frac{3}{2}h - \frac{2kw}{a} + \frac{7}{4}l)] + \\
&\quad \exp[i\pi (\frac{h}{2} + \frac{2kw}{a} + \frac{7}{4}l)] + \\
&\quad \exp[i\pi (\frac{1}{2}a-w) + \frac{3}{2}k + \frac{5}{4}l)] + \\
&\quad \exp[i\pi (\frac{2h}{a}(w + \frac{1}{2}a) + \frac{k}{2} + \frac{5}{4}l)] + \\
&\quad \exp[i\pi (\frac{h}{2} + \frac{2k}{a}(\frac{1}{2}a-w) + \frac{3}{4}l)] + \\
&\quad \exp[i\pi (\frac{3h}{2} + \frac{2k}{a}(w + \frac{1}{2}a) + \frac{3}{4}l)]
\end{aligned}$$

$$\text{Total Structure factor: } S(\vec{K}) = S_{Cd} + S_{Sn} + .3 S_p$$

$$\text{Relative amplitude of diffraction peak: } \text{Amp} = |S(\vec{K})|^2$$

Amp (hkl) < 1.0: disallowed (hkl) peaks

Amp (hkl) > 1.0: Allowed (hkl) peaks